



Conductive Self-Assembled Monolayers of Paramagnetic $\{\text{Co}^{\text{II}}\text{Co}_4^{\text{III}}\}$ and $\{\text{Co}_4^{\text{II}}\text{Co}_2^{\text{III}}\}$ Coordination Clusters on Gold Surfaces

Sebastian Schmitz^{1,2}, Xinkai Qiu³, Maria Glöb^{1,4}, Jan van Leusen¹, Natalya V. Izarova⁴, Muhammad Arif Nadeem⁵, Jan Griebel², Ryan C. Chiechi^{3*}, Paul Kögerler^{1,4*} and Kirill Yu. Monakhov^{2*}

¹ Institut für Anorganische Chemie, RWTH Aachen University, Aachen, Germany, ² Leibniz Institute of Surface Engineering (IOM), Leipzig, Germany, ³ Stratingh Institute for Chemistry, Zernike Institute for Advanced Materials, University of Groningen, Groningen, Netherlands, ⁴ Jülich-Aachen Research Alliance (JARA-FIT), Peter Grünberg Institute, Forschungszentrum Jülich GmbH, Jülich, Germany, ⁵ Department of Chemistry, Quaid-i-Azam University, Islamabad, Pakistan

OPEN ACCESS

Edited by:

Carlos Lodeiro,
New University of Lisbon, Portugal

Reviewed by:

Marius Andruh,
University of Bucharest, Romania
Spyros Panagiotis Perlepes,
University of Patras, Greece

*Correspondence:

Ryan C. Chiechi
r.c.chiechi@rug.nl
Paul Kögerler
paul.koegerler@ac.rwth-aachen.de
Kirill Yu. Monakhov
kirill.monakhov@iom-leipzig.de

Specialty section:

This article was submitted to
Inorganic Chemistry,
a section of the journal
Frontiers in Chemistry

Received: 21 August 2019

Accepted: 01 October 2019

Published: 05 November 2019

Citation:

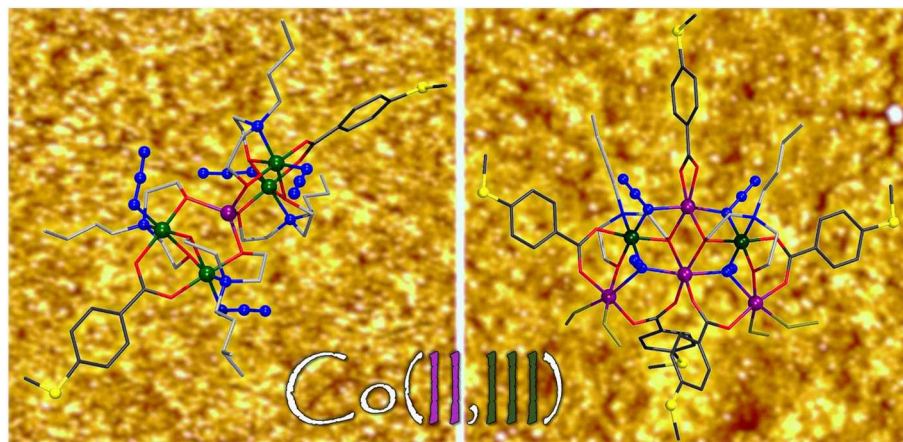
Schmitz S, Qiu X, Glöb M, van Leusen J, Izarova NV, Nadeem MA, Griebel J, Chiechi RC, Kögerler P and Monakhov KY (2019) Conductive Self-Assembled Monolayers of Paramagnetic $\{\text{Co}^{\text{II}}\text{Co}_4^{\text{III}}\}$ and $\{\text{Co}_4^{\text{II}}\text{Co}_2^{\text{III}}\}$ Coordination Clusters on Gold Surfaces. *Front. Chem.* 7:681. doi: 10.3389/fchem.2019.00681

Two polynuclear cobalt(II,III) complexes, $[\text{Co}_5(\text{N}_3)_4(\text{N}-n\text{-bda})_4(\text{bza}\cdot\text{SMe})_2]$ (**1**) and $[\text{Co}_6(\text{N}_3)_4(\text{N}-n\text{-bda})_2(\text{bza}\cdot\text{SMe})_5(\text{MeOH})_4]\text{Cl}$ (**2**), where $\text{Hbza}\cdot\text{SMe} = 4\text{-}(\text{methylthio})\text{benzoic acid}$ and $\text{N}-n\text{-H}_2\text{bda} = \text{N}-n\text{-butyldiethanolamine}$, were synthesized and fully characterized by various techniques. Compound **1** exhibits an unusual, approximately C_2 -symmetric $\{\text{Co}^{\text{II}}\text{Co}_4^{\text{III}}\}$ core of two isosceles Co_3 triangles with perpendicularly oriented planes, sharing a central, high-spin Co^{II} ion residing in a distorted tetrahedral coordination environment. This central Co^{II} ion is connected to four outer, octahedrally coordinated low-spin Co^{III} ions *via* oxo bridges. Compound **2** comprises a semi-circular $\{\text{Co}_4^{\text{II}}\text{Co}_2^{\text{III}}\}$ motif of four non-interacting high-spin Co^{II} and two low-spin Co^{III} centers in octahedral coordination environments. Self-assembled monolayers (SAMs) of **1** and **2** were physisorbed on template-stripped gold surfaces contacted by an eutectic gallium-indium (EGaIn) tip. The acquired current density-voltage (*I*-*V*) data revealed that the cobalt-based SAMs are more electrically robust than those of the previously reported dinuclear $\{\text{Cu}^{\text{II}}\text{Ln}^{\text{III}}\}$ complexes with $\text{Ln} = \text{Gd, Tb, Dy, or Y}$ (Schmitz et al., 2018a). In addition, between 170 and 220°C, the neutral, mixed-valence compound **1** undergoes a redox modification, yielding a $\{\text{Co}_5\}$ -based coordination cluster (**1-A**) with five non-interacting, high-spin octahedral Co^{II} centers as indicated by SQUID magnetometry analysis in combination with X-ray photoelectron spectroscopy and infrared spectroscopy. Solvothermal treatment of **1** results in a high-nuclearity coordination cluster, $[\text{Co}_{10}(\text{N}_3)_2(\text{N}-n\text{-bda})_6(\text{bza}\cdot\text{SMe})_6]$ (**3**), containing 10 virtually non-interacting high-spin Co^{II} centers.

Keywords: cobalt, magnetochemistry, gold surface, molecular conductivity, eutectic gallium-indium electrode

INTRODUCTION

The implementation of metal coordination complexes with specific paramagnetic and/or redox properties as single molecules or as constituents of two-dimensional molecular monolayers (Yao et al., 2019) into computer memory cells (Linnenberg et al., 2018) is a promising way to keep the miniaturization and sustainability of electronic components from colliding with



GRAPHICAL ABSTRACT | The synthesis, structure, magnetochemistry and adsorption behavior of several new cobalt coordination clusters on gold surfaces are reported.

the so-called “quantum limit” (sub-10-nm regime) valid. At both these levels of molecule–surface interfaces, preservation of the main molecular characteristics (Mitcov et al., 2019) as identified in the bulk state, and avoidance of the agglomerative behavior of coordination compounds after their immobilization on solid support constitute important milestones in the controlled (micro-)spectroscopic addressing of the tunnel junction structures of molecule–electrode hybrid devices. The eventual step to practical devices (Sun et al., 2014) mandates an in-depth understanding of the adsorption, autonomous self-organization, electron charge-/spin-transport characteristics (Al-Owaedi et al., 2017; Bu et al., 2018) and switching mechanisms of mono- and polynuclear complexes of transition metals (Higgins and Nichols, 2018), lanthanides (Dreiser, 2015), and their mixed-metal derivatives (Schmitz et al., 2018a) on conductive and semi-conductive surfaces (Cornia et al., 2011).

Based on our ongoing interest in investigating the large-area charge transport properties of moisture-stable polynuclear transition metal complexes, we describe herein the synthesis, structure, and magnetochemistry of novel mixed-valent $\text{Co}^{\text{II/III}}$ and mono-valent Co^{II} coordination clusters and assess their abilities to exhibit reproducible electrical conductivity features when deposited on a metallic substrate. The present study is motivated by the appealing electron transport features and the Kondo effect (Yan and Seminario, 2005; Parks et al., 2010) of mononuclear complexes of an octahedrally coordinated cobalt ion attached to gold electrodes *via* thiol bonds. The augmentation of our polynuclear complexes with ancillary groups like thioethers (Dreiser et al., 2015; Schmitz et al., 2018c) aims to contribute to their conformational and charge stabilization on metallic surfaces and, furthermore, to reduce their possible agglomeration due to steric repulsion between the structurally exposed –SR anchor points. It is however noteworthy that metal complexes derivatized by thiane functionalities as, for example, mononuclear copper(II) pyridyl–alcohol complexes are capable of featuring close intermolecular S⋯S contacts in the crystal lattice (Schmitz et al., 2019).

In the elaborated two-terminal model cell setup the prepared, solution-processable cobalt compounds were adsorbed on an air-stable gold surface as bottom electrode and contacted by a Ga_2O_3 -terminated EGaIn top electrode (Reus et al., 2012), a method that allows the formation of self-assembled monolayers (Wang et al., 2011) (hereinafter referred to as SAMs) and the examination of electron transport through electrically accessible metal centers. The SAM’s morphology, thickness, and current density–voltage characteristics were effectively interpreted using a combination of atomic force microscopy (AFM), scanning tunneling microscopy (STM), and ellipsometry. The findings obtained by these analyses are compared to those reported by us for thioether–Schiff base (L) supported $[\text{CuLn}(\text{L}\cdot\text{SMe})_2(\text{OOCMe})_2(\text{NO}_3)]$ complexes with Ln = Gd, Tb, Dy, or Y (Schmitz et al., 2018a).

EXPERIMENTAL

Materials and Methods

The synthesis of compounds **1–3** was carried out under aerobic conditions. All starting materials were commercial and used as received. Solvents were used without further purification. Elemental analyses were performed using a Vario EL elemental analyzer to determine the C, H, N, and S (deviation ± 0.05) composition in the polycrystalline samples of compounds **1**, **1-A**, and **2** and using an Elementar Vario EL III for the C, H, and N determination of the polycrystalline sample of compound **3**. IR spectra of solid samples were recorded on Nicolet Avatar 360 (**1**, **1-A**, and **2**) and Bruker TENSOR II (**3**) FTIR spectrometers using KBr pellets ($m_{\text{KBr}} \approx 250$ mg) in the range $\tilde{\nu} = 4000\text{--}400$ cm^{-1} . TG/DTA curves of compounds **1–3** were obtained under a nitrogen flux (**1** and **2**) and under a flow of dry air (**1** and **3**) with a heating rate of 5 K min^{-1} in the temperature range $25\text{--}800^\circ\text{C}$ by using a Mettler Toledo TGA/SDTA 851e instrument. The thermally dependent EI-MS of compound **1** was recorded on a Shimadzu GCMS-QP2010S equipped with a Direct Sample Inlet Device DI-2010. The ESI mass spectrometry patterns of

compounds **1** and **2** in the positive ion mode were recorded on a 4000 QTRAP mass spectrometer system by using the LC/LC-MS method with direct infusion.

Synthesis of $[\text{Co}^{\text{II}}\text{Co}^{\text{III}}(\text{N}_3)_4(\text{N}-n\text{-bda})_4(\text{bza}\cdot\text{SMe})_2]\cdot\text{H}_2\text{O}$ (**1**)

$\text{Co}(\text{OOCMe})_2\cdot 4\text{H}_2\text{O}$ (0.250 g, 1.0 mmol) (alternatively, 1.0 mmol of $\text{CoSO}_4\cdot 7\text{H}_2\text{O}$), NaN_3 (0.065 g, 1.0 mmol), and 4-(methylthio)benzoic acid (0.168 g, 1.0 mmol) were dissolved in 6 ml of MeOH to afford the violet mixture. 0.170 ml (1.0 mmol) of *N-n*-butyldiethanolamine was then added. The reaction mixture was stirred under reflux for 3 h and filtered off, and the MeOH filtrate was kept in a capped vial at room temperature. The color of the solution changed from violet to green, and dark-green block-shaped crystals of compound **1** were formed after 3 weeks. The crystals were isolated and washed with ice-cold MeOH. Yield of air-dried crystals: 0.122 g (42% based on Co). **Elemental analysis:** calcd. for $[\text{Co}^{\text{II}}\text{Co}^{\text{III}}(\text{N}_3)_4(\text{N}-n\text{-bda})_4(\text{bza}\cdot\text{SMe})_2]\cdot 1.75\text{H}_2\text{O}$ ($\text{C}_{48}\text{H}_{85.5}\text{Co}_5\text{N}_{16}\text{O}_{13.75}\text{S}_2$, 1,465.58 g mol⁻¹): C, 39.34; H, 5.88; N, 15.29 and S, 4.38%. Found: C, 39.30; H, 5.85; N, 15.50 and S, 4.20%. **IR** (KBr pellet, $\tilde{\nu}_{\text{max}}/\text{cm}^{-1}$): 3,440 (s, br), 2,955 (m), 2,927 (m, sh), 2,867 (m), 2,020 (s), 1,632 (w, sh), 1,580 (m), 1,539 (m), 1,439 (w), 1,408 (s), 1,384 (w, sh), 1,287 (w), 1,185 (w), 1,089 (w, sh), 1,067 (m), 1,030 (w), 1,013 (w), 979 (w), 917 (m), 863 (w), 845 (w), 767 (m), 684 (w), 653 (w), 602 (w), 574 (w), 519 (m), 483 (w). **MS** (MeOH, ESI, m/z): 1,456.231 (measured), 1,456.229 (calcd. for $\text{C}_{48}\text{Co}_5\text{H}_{82}\text{N}_{16}\text{NaO}_{12}\text{S}_2^+$, 100%, $[\text{NaCo}^{\text{II}}\text{Co}^{\text{III}}(\text{N}_3)_4(\text{N}-n\text{-bda})_4(\text{bza}\cdot\text{SMe})_2]^+ + \text{Na}^+$).

Preparation of $[\text{Co}_5^{\text{II}}(\text{N}_3)_2(\text{N}-n\text{-bda})_2(\text{bae})_2(\text{bza}\cdot\text{SMe})_2]\cdot 1.5\text{H}_2\text{O}$ (**1-A**)

The dark-green polycrystalline compound **1** was gradually heated up to 220°C for 15 min in a N₂ flow, which resulted in a violet microcrystalline powder that was subjected to further characterization. The resulting product was however not suitable for X-ray diffraction analysis. **Elemental analysis:** calcd. for $[\text{Co}_5^{\text{II}}(\text{N}_3)_2(\text{N}-n\text{-bda})_2(\text{bae})_2(\text{bza}\cdot\text{SMe})_2]\cdot 1.5\text{H}_2\text{O}$ (Hbae = 2-(butylamino)ethan-1-ol) ($\text{C}_{44}\text{Co}_5\text{H}_{76}\text{N}_{10}\text{O}_{10}\text{S}_2\cdot 1.5\text{H}_2\text{O}$, 1,290.95 g mol⁻¹): C, 40.94; H, 6.17; N, 10.85 and S, 4.97%. Found: C, 41.10; H, 5.63; N, 10.13; and S, 4.84%. **IR** (KBr pellet, $\tilde{\nu}_{\text{max}}/\text{cm}^{-1}$): 3,424 (m, br), 2,954 (s), 2,926 (m, sh), 2,871 (m, sh), 2,057 (s), 1,593 (s), 1,534 (s), 1,495 (w), 1,422 (s), 1,317 (w), 1,270 (w), 1,182 (m), 1,076 (s), 1,039 (w, sh), 1,016 (w, sh), 985 (w), 892 (m), 858 (m), 769 (m), 692 (w), 619 (w), 580 (w), 533 (w), 508 (w), 471 (w).

Synthesis of $[\text{Co}_4^{\text{II}}\text{Co}_2^{\text{III}}(\text{N}_3)_4(\text{N}-n\text{-bda})_2(\text{bza}\cdot\text{SMe})_5(\text{MeOH})_4]\text{Cl}\cdot 2.25\text{MeOH}$ (**2**)

Compound **2** was prepared following the protocol for the synthesis of compound **1**, but using $\text{CoCl}_2\cdot 6\text{H}_2\text{O}$ (0.238 g, 1.0 mmol) instead of $\text{Co}(\text{OOCMe})_2\cdot 4\text{H}_2\text{O}$. Yield of air-dried crystals: 0.057 g (19% based on Co). **Elemental analysis:** calcd. for $[\text{Co}_4^{\text{II}}\text{Co}_2^{\text{III}}(\text{N}_3)_4(\text{N}-n\text{-bda})_2(\text{bza}\cdot\text{SMe})_5]\text{Cl}\cdot 8\text{H}_2\text{O}$

($\text{C}_{56}\text{Cl}_1\text{Co}_6\text{H}_{85}\text{N}_{14}\text{O}_{22}\text{S}_5$, 1,855.73 g mol⁻¹): C, 36.24; H, 4.62; N, 10.57 and S, 8.64%. Found: C, 35.99; H, 4.10; N, 10.65; and S, 8.35%. **IR** (KBr pellet, $\tilde{\nu}_{\text{max}}/\text{cm}^{-1}$): 3,427 (s, br), 2,959 (m), 2,924 (m), 2,871 (w), 2,087 (vs), 1,593 (s), 1,540 (m), 1,403 (s), 1,286 (m), 1,257 (w, sh), 1,216 (w), 1,184 (m), 1,089 (m), 1,014 (w), 967 (w), 925 (w), 847 (w), 771 (m), 693 (w), 633 (w), 581 (w), 517 (w), 479 (m). **MS** (MeOH, ESI, m/z): 1,675.019 (measured), 1,674.974 (calcd. for $\text{C}_{56}\text{Co}_6\text{H}_{69}\text{N}_{14}\text{O}_{14}\text{S}_5^+$, 100%; $[\text{Co}_6(\text{N}_3)_4(\text{N}-n\text{-bda})_2(\text{bza}\cdot\text{SMe})_5]^+ - 4\text{MeOH}$).

Synthesis of $[\text{Co}_{10}^{\text{II}}(\text{N}_3)_2(\text{N}-n\text{-bda})_6(\text{bza}\cdot\text{SMe})_6]$ (**3**)

Freshly prepared and dried polycrystalline compound **1** (0.050 g, 0.035 mmol) was dissolved in 5 ml of DMSO and pyrazine was added as a crystallization reagent (0.030 g, 0.375 mmol). The resulting green solution was placed in an autoclave-stable glass vial and reacted in an oven at 100°C for 120 h under autogenous pressure. The reaction solution was cooled down to room temperature over 4 h. Pink single crystals of **3** were collected by filtration, washed with ice-cold EtOH, and dried in air. Yield of air-dried crystals: 0.011 g (24% based on Co). Please note that the synthesis is also successful in the absence of pyrazine, but the yield of crystalline product is much lower. **Elemental analysis:** calcd. for $[\text{Co}_{10}^{\text{II}}(\text{N}_3)_2(\text{N}-n\text{-bda})_6(\text{bza}\cdot\text{SMe})_6]\cdot 0.7\text{pyrazine}\cdot 6\text{H}_2\text{O}$ ($\text{Co}_{10}\text{C}_{96}\text{H}_{144}\text{N}_{12}\text{O}_{24}\text{S}_6\cdot 0.7\text{pyrazine}\cdot 6\text{H}_2\text{O}$, 2,631.95 g mol⁻¹, disregarding solvent molecules): C, 42.44; H, 5.72; and N, 6.71%. Found: C, 42.32; H, 5.35 and N, 7.04%. **IR** (KBr pellet, $\tilde{\nu}_{\text{max}}/\text{cm}^{-1}$): 3,442 (m, br), 2,954 (m), 2,926 (m, sh), 2,871 (m), 2,853 (m, sh), 2,058 (vs), 1,593 (s), 1,534 (s), 1,496 (w), 1,463 (w, sh), 1,422 (vs), 1,384 (w, sh), 1,317 (w), 1,270 (w), 1,182 (w), 1,136 (vw), 1,091 (m), 1,076 (s), 1,040 (m, sh), 1,017 (m, sh), 985 (w), 968 (vw), 909 (w), 888 (w), 857 (m), 769 (m), 713 (vw), 693 (w), 669 (vw), 631 (vw), 579 (w), 534 (w), 508 (vw), 474 (w), 419 (w).

X-Ray Crystallography

Single-crystal diffraction data for **1–3** were collected on a SuperNova (Agilent Technologies) diffractometer with MoK α radiation ($l = 0.71073$ Å) at 120 K (for **1** and **2**) and on a Bruker APEX II CCD diffractometer at 100 K (for **3**). The crystals were mounted in a Hampton cryoloop with Paratone-N oil to prevent water loss. Absorption corrections were applied either analytically based on multifaceted crystal model using CrysAlis software (**1**, **2**)¹ or empirically using the SADABS program (**3**)². The structures were solved by direct methods and refined by full-matrix least-squares method against $|F|^2$ with anisotropic thermal parameters for all non-hydrogen atoms (Co, S, O, N, C, and Cl) using the SHELXTL software package (Sheldrick, 2015). Hydrogen atoms were placed in geometrically calculated positions. Hydrogen atoms of the disordered solvent molecules (e.g., H₂O in **1** and MeOH in **2**), OH groups of the MeOH ligands

¹CrysAlisPro, Agilent Technologies, Version 1.171.36.28 (release 01-02-2013 CrysAlis171.NET) (compiled Feb 1 2013, 16:14:44) (Clark and Reid, 1995).

²APEX2 (Version 1.08), SAINT (Version 7.03), SADABS (Version 2.11). Bruker Advanced X-Ray Solutions, Madison (WI, USA).

in **2**, and the disordered $-\text{CH}_2-\text{CH}_3$ moiety of one of the N - n -bda²⁻ ligands in **1** and the disordered $-\text{Me}$ group of one of the methanol ligands in **2** were not located.

The structure of **1** was refined as a two-component twin ($-1\ 0\ 0; 0\ -1\ 0; 0\ 0\ -1$; BASF 0.52). The relative site occupancy factors for the disordered positions of carbon and oxygen atoms in **1** and in **2** were refined using a combination of PART/EADP or PART/EADP/SUMP instructions.

Additional crystallographic data are summarized in **Table S1**. Further details on the crystal structure investigation can be obtained, free of charge, on application to CCDC, 12 Union Road, Cambridge CB2 1EZ, UK: <http://www.ccdc.cam.ac.uk/>, e-mail: data_request@ccdc.cam.ac.uk, or fax: +441223 336033 upon quoting 1936117 (**1**), 1936118 (**2**), and 1936119 (**3**) numbers.

XPS Measurements

XPS measurements were carried out using a PHI 5000 Versa Probe (Physical Electronics Inc., USA) under ultra-high vacuum conditions (1×10^{-9} mbar). The samples were excited with monochromatic Al K_{α} X-rays (1486.6 eV). The energy analyzer operates with a pass energy of 29.35 eV. The take-off angle between the analyzer and the sample was 45° . CasaXPS was used to analyze the spectra. To compensate charging effects, the binding energies were referenced to the C 1s peak at 284.8 eV. The spectra were performed by fitting a convolution of a Lorentzian profile and a Gaussian profile after subtraction of a Shirley background.

Magnetic Susceptibility Measurements

Magnetic susceptibility data of compounds **1**, **1-A**, **2**, and **3** were recorded using a Quantum Design MPMS-5XL SQUID magnetometer for direct current (dc) and alternating current (ac) measurements. The polycrystalline samples were compacted and immobilized into PTFE capsules. The dc susceptibility data were acquired as a function of the field (0.1–5.0 T) and temperature (2.0–290 K). The ac susceptibility data were measured in the absence of a static bias field in the frequency range 3–1,000 Hz ($T = 2.0$ – 50.0 K, $B_{ac} = 3$ G), but no out-of-phase signals were observed. The data were corrected for diamagnetic contributions from the sample holders and the compounds [$\chi_{m, \text{dia}}/10^{-4}$ cm³ mol⁻¹ = -7.17 (**1**); -6.41 (**1-A**); -9.92 (**2**); -13.2 (**3**)]. For the compounds containing octahedrally coordinated, low-spin Co^{III} centers, data were additionally corrected for their TIP contributions (Cossee, 1958) [$\chi_{m, \text{TIP}}/10^{-4}$ cm³ mol⁻¹ = $+1.59$ (**1**); $+0.80$ (**2**)].

Preparation of the Self-Assembled Monolayers

SAMs of compounds **1** and **2** were prepared by incubating freshly cleaved 1×1 cm² Au^{TS} substrates in 5 ml of 0.1 mM methanolic solution of each metal complex overnight. The substrates were then rinsed with methanol (3×1 ml) and the residual solvent on the surface was removed under a stream of dry N₂. The samples were used for measurements and analysis immediately.

EGaIn Measurements

Electrical measurements with EGaIn were performed under ambient conditions. In the measurements, each sample was grounded and the EGaIn was biased. At least three samples were examined for the SAMs of compounds **1** and **2**. The potential windows include the following: $0\ \text{V} \rightarrow 1\ \text{V} \rightarrow -1\ \text{V} \rightarrow 0\ \text{V}$, steps of 0.05 V. A total of 5 trace/retrace cycles were recorded for each junction, and shorts that occurred during the measurement (short upon contact with a bias of 1 V or during the cycle) were counted for the failure of a junction.

AFM Measurements

PeakForce Tapping AFM measurements were performed on a Bruker AFM multimode MMAFM-2 model. Pure SAMs of compounds **1** and **2** and freshly cleaved Au^{TS} substrates were characterized by AFM on morphology. The PeakForce Tapping AFM was performed with a ScanAsyst-Air probe (resonant frequency 70 kHz, spring constant 0.4 N/m, Bruker) to characterize the surface morphology of the samples at a scan rate of 0.8 Hz and 768 samples per line. The data were analyzed with Nanoscope Analysis 1.5 provided by Bruker.

Ellipsometry

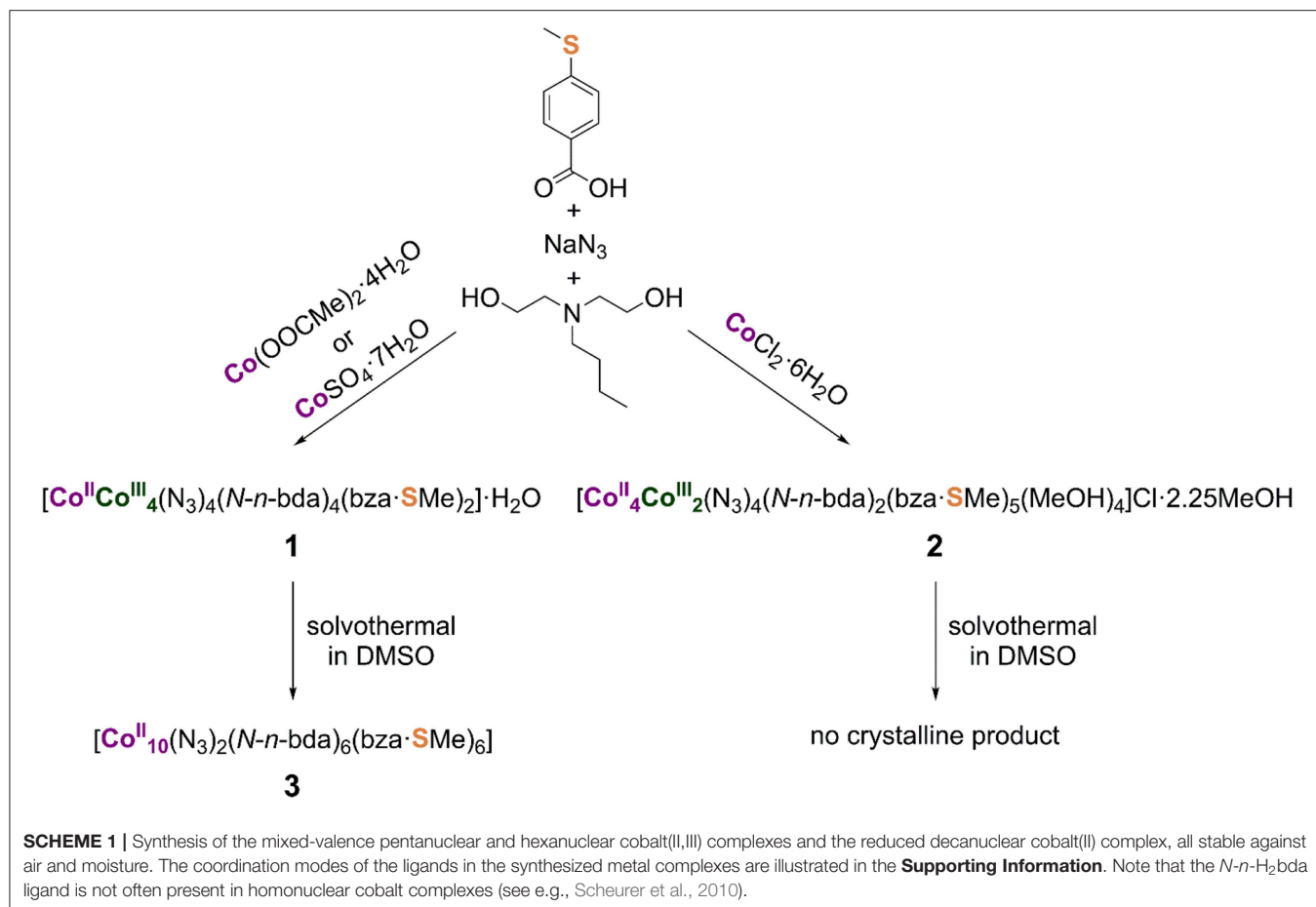
Ellipsometry measurements were carried out in air by using a V-Vase Rotating Analyzer equipped with a HS-190 monochromator ellipsometer from J.A. Woollam Co., Inc. A two-layer model consisting of a bottom Au layer, for which optical constants were calculated from freshly prepared template stripped Au surfaces, and a Cauchy layer was used for the fit of the measurements on the SAMs. A chosen value of $n = 1.45$ and $k = 0$ at all wavelengths (i.e., Cauchy parameter $A_n = 1.45$, $B_n = C_n = 0$) was used to fit the thickness.

RESULTS AND DISCUSSION

Synthesis and Mass-Spectrometric Characterization

Compounds **1** and **2** were synthesized *via* one-pot aerobic reactions summarized in **Scheme 1**. The choice of cobalt precursor under otherwise identical reaction conditions is key to the isolation of the desired compound. In the general reaction procedure, a cobalt(II) salt and 4-(methylthio)benzoic acid (Hbza-SMe) were dissolved in methanol together with N - n -butyldiethanolamine (N - n -H₂bda) and sodium azide (NaN₃) as co-ligands. All reactants were used in an equimolar ratio. The resulting violet solution was stirred under reflux for 2 h and then worked up (see Experimental section for more details).

Compound **1**, [Co^{II}Co^{III}(N₃)₄(N - n -bda)₄(bza-SMe)₂].H₂O, forms in the presence of cobalt(II) acetate-tetrahydrate (Co(OOCMe)₂·4H₂O) or cobalt(II) sulfate-heptahydrate (CoSO₄·7H₂O). The dark-green, block-shaped crystals of neutral compound **1** are highly soluble in CHCl₃, CH₂Cl₂, and tetrahydrofuran (THF); moderately soluble in acetone; and poorly soluble in MeOH, EtOH, and MeCN. The positive-mode electrospray ionization (ESI) mass spectrum of a methanol solution of **1** (see **Supporting Information** for details) contains peaks that correspond to the singly and quadruply charged



sodium adduct ions (Maloth et al., 2015) $[\text{NaCo}^{\text{II}}\text{Co}_4^{\text{III}}(\text{N}_3)_4(\text{N-n-bda})_4(\text{bza}\cdot\text{SMe})_2]^+$ at m/z 1,456 and $[\text{Na}_4\text{Co}^{\text{II}}\text{Co}_4^{\text{III}}(\text{N}_3)_4(\text{N-n-bda})_4(\text{bza}\cdot\text{SMe})_2]^{4+}$ with 100% intensity at m/z 381, respectively. The signal of $[\text{Co}_4^{\text{II}}\text{Co}^{\text{III}}(\text{N}_3)_4(\text{N-n-bda})_3(\text{bza}\cdot\text{SMe})_2(\text{H}_2\text{O})(\text{H}^+)]^{2+}$ at m/z 647 and those of the coordination cluster ions with different amounts of azide groups $[\text{Co}^{\text{II}}\text{Co}_4^{\text{III}}(\text{N}_3)_3(\text{N-n-bda})_4(\text{bza}\cdot\text{SMe})_2]^+$ at m/z 1,391, $[\text{Co}_2^{\text{II}}\text{Co}_3^{\text{III}}(\text{N}_3)_2(\text{N-n-bda})_4(\text{bza}\cdot\text{SMe})_2]^+$ at m/z 1,349, $[\text{Co}_3^{\text{II}}\text{Co}_2^{\text{III}}(\text{N}_3)(\text{N-n-bda})_4(\text{bza}\cdot\text{SMe})_2]^+$ at m/z 1,307, and $[\text{Co}_4^{\text{II}}\text{Co}^{\text{III}}(\text{N-n-bda})_4(\text{bza}\cdot\text{SMe})_2]^+$ at m/z 1,265 are also observed. As can be seen for the singly charged ions, cobalt(III) centers undergo partial reduction to Co^{II} upon loss of azides during the ionization process. This indicates that the $[\text{Co}^{\text{II}}\text{Co}_4^{\text{III}}(\text{N}_3)_4(\text{N-n-bda})_4(\text{bza}\cdot\text{SMe})_2]$ complex (**1**) could, in principle, be converted to a reduced $\{\text{Co}_5\}$ -based derivative. Elemental analysis of compound **1** emphasizes the stability of the complex against air and moisture, although **1** takes up a small amount of water during drying and storing under ambient conditions ($[\text{Co}^{\text{II}}\text{Co}_4^{\text{III}}(\text{N}_3)_4(\text{N-n-bda})_4(\text{bza}\cdot\text{SMe})_2]\cdot 1.75\text{H}_2\text{O}$ vs. $[\text{Co}^{\text{II}}\text{Co}_4^{\text{III}}(\text{N}_3)_4(\text{N-n-bda})_4(\text{bza}\cdot\text{SMe})_2]\cdot\text{H}_2\text{O}$ as determined crystallographically).

Compound **2**, $[\text{Co}_4^{\text{II}}\text{Co}_2^{\text{III}}(\text{N}_3)_4(\text{N-n-bda})_2(\text{bza}\cdot\text{SMe})_5(\text{MeOH})_4]\text{Cl}\cdot 2.25\text{MeOH}$, forms when cobalt(II) chloride-hexahydrate ($\text{CoCl}_2\cdot 6\text{H}_2\text{O}$) was utilized.

The dark-green, plate-like crystals of ionic compound **2** are soluble in CH_2Cl_2 , THF, acetone, and MeCN; moderately soluble in MeOH and EtOH; and insoluble in water. The positive-mode ESI mass spectrometry pattern of a methanol solution of **2** (see **Supporting Information** for details) shows the signal at m/z 1,675 with 100% intensity, which is assigned to the singly charged ion of $[\text{Co}_4^{\text{II}}\text{Co}_2^{\text{III}}(\text{N}_3)_4(\text{N-n-bda})_2(\text{bza}\cdot\text{SMe})_5]^+$ after the loss of four coordinated MeOH molecules. Isotopic patterns reflecting reduction processes as in neutral complex **1** with terminal azide groups were not observed for ionic complex **2** with bridging azide groups, thus revealing **2** as less reactive. Elemental analysis of **2** indicates the stability of the central $[\text{Co}_4^{\text{II}}\text{Co}_2^{\text{III}}(\text{N}_3)_4(\text{N-n-bda})_2(\text{bza}\cdot\text{SMe})_5]^+$ molecular framework against air and moisture, although **2** loses the four weakly coordinated MeOH molecules and the uncoordinated crystal solvent by an uptake of water molecules during drying and storing under ambient conditions ($[\text{Co}_4^{\text{II}}\text{Co}_2^{\text{III}}(\text{N}_3)_4(\text{N-n-bda})_2(\text{bza}\cdot\text{SMe})_5]\text{Cl}\cdot 8\text{H}_2\text{O}$ vs. $[\text{Co}_4^{\text{II}}\text{Co}_2^{\text{III}}(\text{N}_3)_4(\text{N-n-bda})_2(\text{bza}\cdot\text{SMe})_5(\text{MeOH})_4]\text{Cl}\cdot 2.25\text{MeOH}$ as determined crystallographically). The loss of the neutral coordinated solvent molecules was also identified in the ESI-MS pattern of **2**.

The reactivity of compounds **1** and **2** was tested under solvothermal conditions (**Scheme 1**). Each compound was dissolved in DMSO and the resulting green solutions were heated

up to 100°C for 120 h in sealed autoclavable glass vials, followed by slow cooling to room temperature. Contrary to the reaction solution containing **1** yielding pink needle-shaped crystals of $[\text{Co}_{10}^{\text{II}}(\text{N}_3)_2(\text{N}-n\text{-bda})_6(\text{bza}\cdot\text{SMe})_6]$ (**3**), that of compound **2** gave no crystalline product, although **2** can be strikingly compared to the previously synthesized coordination cluster $[\text{Co}_3^{\text{II}}\text{Co}_2^{\text{III}}(\text{N}-n\text{-bda})_2(\text{N}-n\text{-Hbda})_2(\text{ib})_6]$ ($\text{ib}^- = \text{isobutyrate}$) (Schmitz et al., 2016a). Interestingly, the latter complex acts as an indispensable precursor material for the preparation of the previously reported complex $[\text{Co}_{10}^{\text{II}}(\text{OH})_2(\text{N}-n\text{-bda})_6(\text{ib})_6]$ (Schmitz et al., 2018b) that shows similarities to **3** (see Discussion of their molecular structures below). Thus, both $\text{Co}_{10}^{\text{II}}$ complexes can be solvothermally formed from mixed-valence $\text{Co}_5^{\text{II/III}}$ precursors in DMSO.

X-Ray Crystal Structures

The solid-state molecular structures of **1–3** were established by single-crystal X-ray diffraction (see **Supporting Information** for details). Compound **1** crystallizes in the monoclinic space group $P2_1/c$ (**Figure 1**). The structure consists of five cobalt atoms, where four of them reside in an octahedral N_2O_4 environment and exhibit a formal oxidation state of +III as established by bond valence sum (BVS) analysis [$\Sigma_{\text{bv}}(\text{Co}^{\text{III}}) = 3.08\text{--}3.12$]. The fifth cobalt site, located at the center of the molecule, displays a highly distorted tetrahedral geometry and is assigned the formal oxidation state +II [$\Sigma_{\text{bv}}(\text{Co}^{\text{II}}) = 1.72$]. The mixed-valent $\{\text{Co}_5\}$ core is thus similar to that observed in the other known Co_5 complexes (Englert and Strähle, 1987; Ferguson et al., 2006; Funes et al., 2015; Li et al., 2017) and comprises two $\{\text{Co}_2^{\text{III}}\text{Co}^{\text{II}}\}$ triangles that share a common Co^{II} vertex, an $\sim 90^\circ$ angle between the triangle planes. The Co^{III} coordination spheres are composed of one $\text{bza}\cdot\text{SMe}^-$, two $\text{N}-n\text{-bda}^{2-}$, and two azide ligands. The $\text{bza}\cdot\text{SMe}^-$ ligand bridges two Co^{III} ions [$\text{Co}^{\text{III}}\text{--O}_{\text{bza}\cdot\text{SMe}}: 1.919(3)\text{--}1.925(3)$ Å], and each azide coordinates terminally to every Co^{III} ion [$\text{Co}^{\text{III}}\text{--N}_{\text{azide}}: 1.930(4)\text{--}1.940(3)$ Å]. These Co^{III} centers are additionally bridged by oxygen atoms of ethoxide residues of two $\text{N}-n\text{-bda}^{2-}$ ligands [$\text{Co}^{\text{III}}\text{--O}_{\text{bda}}: 1.896(3)\text{--}1.932(3)$ Å]. The other ethoxide groups of each $\text{N}-n\text{-bda}^{2-}$ ligand link the peripheral Co^{III} ions with the central Co^{II} ion through their oxygen atoms [$\text{Co}^{\text{III}}\text{--O}_{\text{bda}}: 1.867(3)\text{--}1.875(3)$ Å; $\text{Co}^{\text{II}}\text{--O}_{\text{bda}}: 1.996(3)\text{--}2.010(3)$ Å]. The non-bonding $\text{Co}^{\text{III}}\cdots\text{Co}^{\text{II}}$ distances range from 3.0834(0) to 3.1116(0) Å, the nearest $\text{Co}^{\text{III}}\cdots\text{Co}^{\text{III}}$ distance is 2.8499(7) Å ($\text{Co1}\cdots\text{Co2}$), and the longest $\text{Co}^{\text{III}}\cdots\text{Co}^{\text{III}}$ is 5.8833(1) Å ($\text{Co1}\cdots\text{Co4}$). The intramolecular distance between two sulfur atoms is *ca.* 22.061 Å. The thioether groups are not involved in any intermolecular coordinative bonds as it was also observed for other complexes with similar ligands (Ghisolfi et al., 2014; Schmitz et al., 2015, 2016b,c).

Compound **2** crystallizes in the orthorhombic space group $Pbca$ and represents an ionic compound consisting of the hexanuclear $[\text{Co}_6(\text{N}_3)_4(\text{N}-n\text{-bda})_2(\text{bza}\cdot\text{SMe})_5(\text{MeOH})_4]^+$ complex charge-balanced by a Cl^- ion (**Figure 2**). Five cobalt atoms exhibiting alternating oxidation states +II and +III [$\Sigma_{\text{bv}}(\text{Co}^{\text{II}}) = 1.9\text{--}2.0$, $\Sigma_{\text{bv}}(\text{Co}^{\text{III}}) = 3.1$] form a semicircular or horseshoe-shaped metal

core structure reminiscent of that previously described complex $[\text{Co}_3^{\text{II}}\text{Co}_2^{\text{III}}(\text{N}-n\text{-bda})_2(\text{N}-n\text{-Hbda})_2(\text{ib})_6]$ (Schmitz et al., 2016a) (see **Supporting Information** for a comparative analysis). However, in **2**, this structural motif is complemented with a centrally accommodated, sixth cobalt(II) atom. The cationic part of compound **2** is supported by five 4-(methylthio)benzoate ligands, two fully deprotonated $\text{N}-n$ -butyldiethanolamine ligands, four azide ions, and four methanol molecules. The presence of the latter suggests interesting derivatization perspectives for this type of cobalt structural motifs unlike the reported $[\text{Co}_3^{\text{II}}\text{Co}_2^{\text{III}}(\text{N}-n\text{-bda})_2(\text{N}-n\text{-Hbda})_2(\text{ib})_6]$ complex. All cobalt ions in **2** adopt an octahedral geometry. The reduced Co2 and Co6 reside in a NO_5 , the oxidized Co3 and Co5 reside in a N_3O_3 , and the reduced Co1 and Co4 reside in a N_2O_4 environment. The central Co1 center is connected to Co2 and Co6 through the μ_3 -azide groups [$\text{Co1}\text{--}\mu_3\text{-N}_{\text{azide}}: 2.203(6)$ and $2.216(7)$ Å] and the carboxylate $\mu_2\text{-COO}^-$ groups of the $\text{bza}\cdot\text{SMe}^-$ ligand [$\text{Co1}\text{--O}_{\text{bza}\cdot\text{SMe}}: 1.974(5)$ and $2.005(5)$ Å]. It is further bridged to Co3 and Co5 *via* the abovementioned μ_3 -azide groups [$\text{Co3}\text{--}\mu_3\text{-N}_{\text{azide}}: 1.982(6)$ and $\text{Co5}\text{--}\mu_3\text{-N}_{\text{azide}}: 1.970(6)$ Å] and the μ_3 -oxygen atoms of the ethoxide groups of the $\text{N}-n\text{-bda}^{2-}$ ligands, which also coordinate to Co4 [$\text{Co}\text{--}\mu_3\text{-O}_{\text{bda}}: 1.907(5)\text{--}2.148(5)$ Å]. In addition, Co4 is linked to Co3 and Co5 by bridging azide groups [$\text{Co}\text{--}\mu_2\text{-N}_{\text{azide}}: 1.947(6)\text{--}2.063(7)$ Å]. The coordination sphere of Co4 is saturated by one chelating $\text{bza}\cdot\text{SMe}^-$ ligand [$\text{Co4}\text{--O}_{\text{bza}\cdot\text{SMe}}: 2.078(5)$ and $2.164(5)$ Å]. The coordination sphere of each Co3 and Co5 is completed by a μ_2 -oxygen atom of the ethoxide group of the $\text{N}-n\text{-bda}^{2-}$ ligand that also connects to Co2 or Co6 [$\text{Co}\text{--}\mu_2\text{-O}_{\text{bda}}: 1.882(5)\text{--}2.013(5)$ Å], and by a nitrogen atom of this ligand [$\text{Co3}\text{--N}_{\text{bda}}: 1.991(6)$ Å and $\text{Co5}\text{--N}_{\text{bda}}: 1.994(6)$ Å]. The structure displays four coordinated methanol molecules where two of them are attached terminally to Co2 and the other two are attached to Co6 [$\text{Co}\text{--O}_{\text{MeOH}}: 2.060(6)\text{--}2.122(5)$ Å]. The peripheral thioether groups are not involved in any intermolecular coordinative bonds (Ghisolfi et al., 2014; Schmitz et al., 2015, 2016b,c).

Compound **3** crystallizes in the monoclinic space group $P2_1/n$ (**Figure 3**) and displays strong structural similarities to the previously reported $[\text{Co}_{10}^{\text{II}}(\text{OH})_2(\text{N}-n\text{-bda})_6(\text{ib})_6]$ (Schmitz et al., 2018b). The main differences between these two neutral coordination clusters concern the two discrete OH^- groups that in the latter are replaced by two bridging N_3^- ligands [$\text{Co}\text{--N}_{\text{azide}}: 2.212(3)$ Å and $2.293(4)$ Å] and the ib ligands, replaced by $\text{bza}\cdot\text{SMe}^-$ in **3** [$\text{Co}\text{--O}_{\text{bza}\cdot\text{SMe}}: 2.028(3)\text{--}2.296(3)$ Å]. Contrary to $[\text{Co}_{10}^{\text{II}}(\text{OH})_2(\text{N}-n\text{-bda})_6(\text{ib})_6]$ with only octahedral cobalt centers, compound **3** features eight octahedral and two (Co2 and Co2') NO_4 -trigonal bipyramidal Co environments. These five-coordinated Co^{II} centers bind only one carboxylic oxygen of $\text{bza}\cdot\text{SMe}^-$ [$2.028(3)$ Å], while the $\text{Co}\cdots\text{O}$ distance for the second center is too long for the bond [$2.722(3)$ Å]. For comparison, the corresponding distances in the known $[\text{Co}_{10}^{\text{II}}(\text{OH})_2(\text{N}-n\text{-bda})_6(\text{ib})_6]$ complex are about 0.3 Å shorter and constitute 2.363(3) Å and 2.466(3) Å. In contrast, the similar $\text{Co}\text{--O}_{\text{bza}\cdot\text{SMe}}$ distance for Co4 is much shorter [$2.296(3)$ Å] and is just slightly above the $\text{Co4}\text{--O}_{\text{bza}\cdot\text{SMe}}$ distance to the second O of the same ligand [$2.160(3)$ Å]. Other structurally characterized

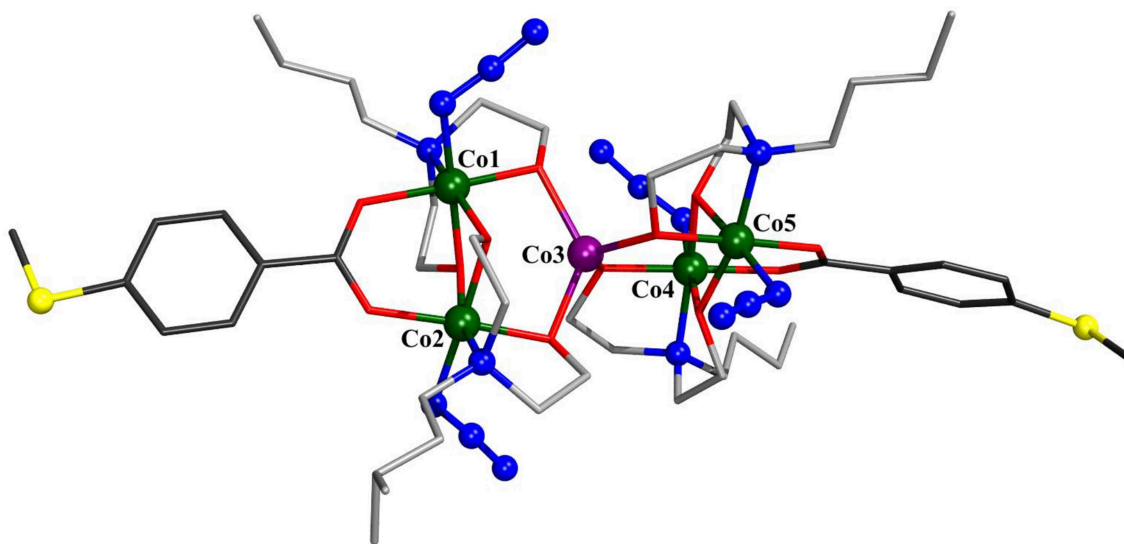


FIGURE 1 | Molecular structure of $[\text{Co}^{\text{II}}\text{Co}^{\text{III}}(\text{N}_3)_4(\text{N}-n\text{-bda})_4(\text{bza-SMe})_2]$ (**1**). Hydrogen atoms and co-crystallized water molecule are omitted for clarity. The cobalt, sulfur, and the nitrogen atoms of azide groups are represented as ball-and-stick models. Color code: C (bza-SMe⁻) = dark gray; C (*N-n-bda*²⁻) = gray; N = blue; O = red; S = yellow; Co^{II} = violet, Co^{III} = dark green. See **Supporting Information** for detailed crystal packing of the complexes.

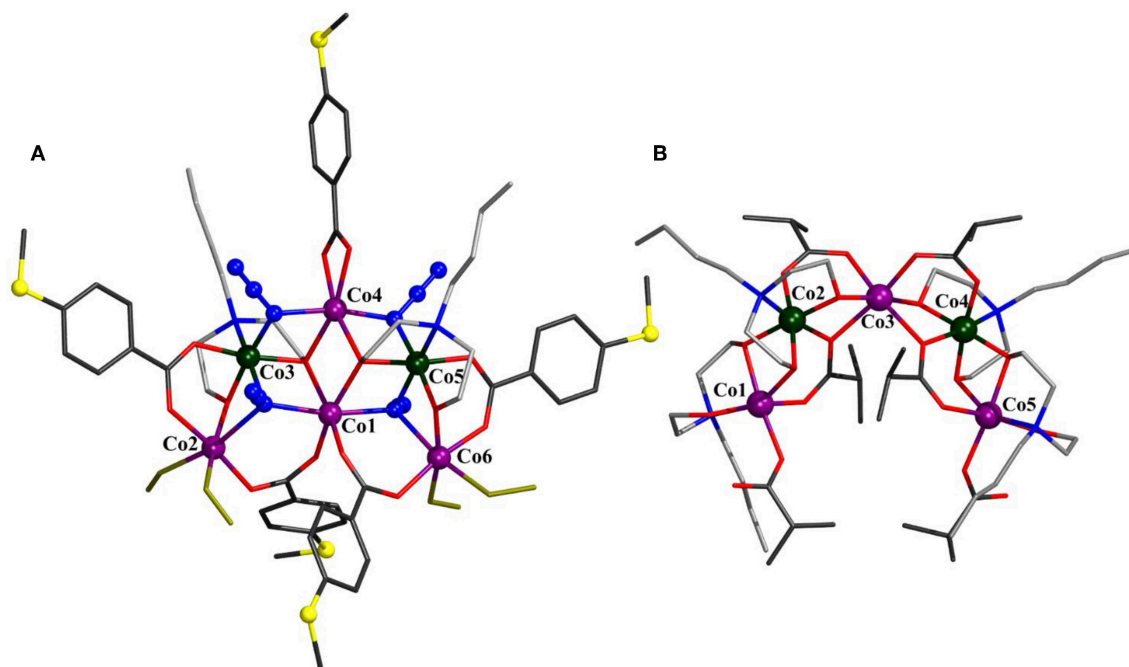


FIGURE 2 | Molecular structure of $[\text{Co}^{\text{II}}\text{Co}^{\text{III}}(\text{N}_3)_4(\text{N}-n\text{-bda})_2(\text{bza-SMe})_5(\text{MeOH})_4]^+$ in **2** (**A**) and comparison to $[\text{Co}^{\text{II}}\text{Co}^{\text{III}}(\text{N}_3)_4(\text{N}-n\text{-bda})_2(\text{N}-n\text{-Hbda})_2(\text{lb})_6]$ (Schmitz et al., 2016a) (**B**). Hydrogen atoms, Cl⁻ counterion, and co-crystallized solvent molecules are omitted for clarity. The cobalt, sulfur, and the nitrogen atoms of azides are represented as ball-and-stick models. Color code: C (carboxylates) = dark gray; C (*N-n-Hbda*⁻ and *N-n-bda*²⁻) = gray; N = blue; O = red; S = yellow; coordinated MeOH molecules = yellow sticks; Co^{II} = violet; Co^{III} = dark green. See **Supporting Information** for detailed crystal packing of the complexes.

decanuclear cobalt coordination clusters are also available (Canaj et al., 2014).

Thermal Treatment of 1

Guided by the ESI-MS spectrum and the TG/DTA curve of compound **1** measured in the temperature range 25–800°C

(see **Supporting Information** for details), this coordination cluster was grinded into the dark-green powder that was selectively heated up to 220°C for 15 min under a nitrogen flow. An exothermic step in the range 170–220°C was observed, corresponding to a weight loss (Δm_{found}) of 11.95% that is assigned to two C₂H₃O⁻ groups (two ethynol and one H₂)

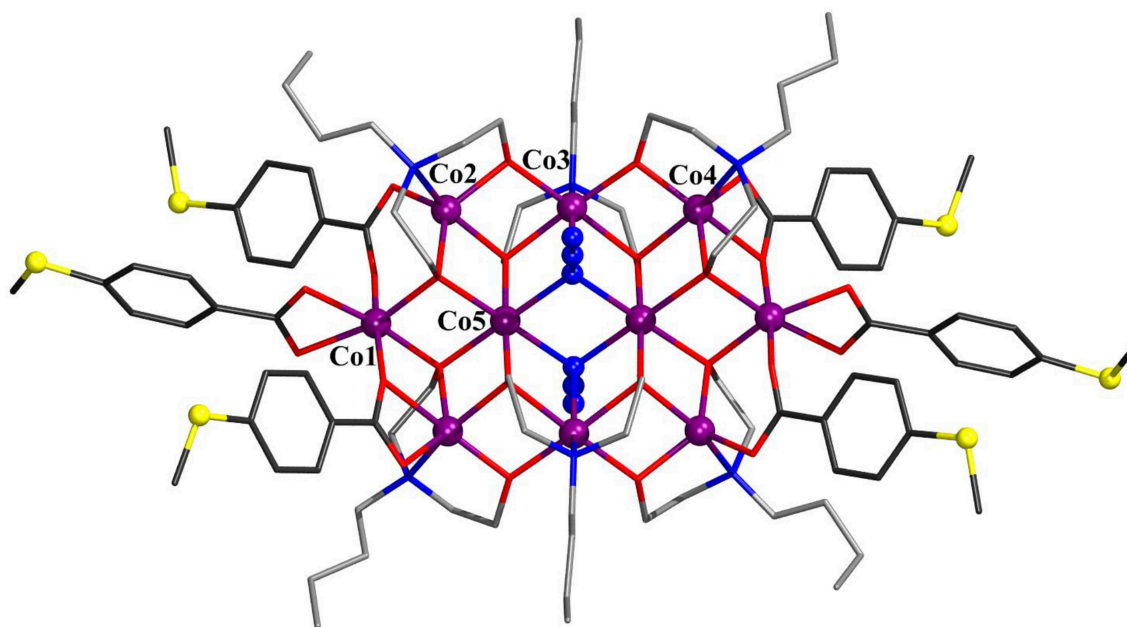


FIGURE 3 | Molecular structure of $[\text{Co}_{10}(\text{N}_3)_2(\text{N}-n\text{-bda})_6(\text{bza-SMe})_6]$ (**3**) with Co numbering scheme for one asymmetric unit. Hydrogen atoms are omitted for clarity. The cobalt, sulfur, and the nitrogen atoms of azides are represented as ball-and-stick models. Color code: C (carboxylates) = dark gray; C ($\text{N}-n\text{-bda}^{2-}$) = gray; N = blue; O = red; S = yellow; Co^{II} = violet. See **Supporting Information** for detailed crystal packing of the complexes.

from the $\text{N}-n\text{-bda}^{2-}$ ligands and to two terminal azide groups ($\Delta m_{\text{calcd.}} = 11.86\%$). The loss of not only N_2 from azides is also supported by thermal mass-spectrometry measurements (see **Supporting Information** for details). The IR spectrum of the thermally-generated, dark-violet compound **1-A** illustrated in **Figure 4** still shows the presence of azide groups, which points out that not all of these ligands were released during the thermal processing of compound **1**. The band shift from $2,020\text{ cm}^{-1}$ (asymmetric stretching vibrations of the terminal coordinated $-\text{N}=\text{N}^+=\text{N}^-$ groups in **1**) to $2,057\text{ cm}^{-1}$ (in **1-A**) indicates that the remaining azide ligands change their coordination mode from terminal to bridging (see **Supporting Information** for detailed description of IR spectra). This $\Delta\tilde{\nu}$ shift of 37 cm^{-1} is in line with the reported $\Delta\tilde{\nu}$ values describing the terminal vs. bridging N_3^- coordination (Ray et al., 2003; Mandal et al., 2017). In addition to this, the elemental analysis of compound **1-A** reveals *ca.* 10% of nitrogen (see Experimental section), which reflects the loss of only two azide groups. Although the IR spectra of compounds **1-A** and **3** are almost identical as seen in **Figure 4**, these compounds exhibit different colors (dark violet vs. pink, respectively) and magnetochemical behavior (see Discussion below). Given that the asymmetric stretching vibration band of azides in **3** appears at $2,058\text{ cm}^{-1}$, the rearrangement of these ligands in **1-A** thus are likely.

The acquired data from TG/DTA, IR, and CHNS analyses were used to propose the structural redox modification route toward **1-A** (**Scheme 2**). The electronic and magnetic characteristics of this compound were further studied by X-ray photoelectron spectroscopy (XPS) and the SQUID method.

XPS Spectrum of Compounds **1** and **1-A**

Figure 5 shows the XPS spectra of bulk **1** and **1-A**. The binding energy of Co $2p_{3/2}$ peak is 779.0 eV for **1** and 779.5 eV for **1-A**. The Co $2p_{1/2}$ peak is shifted by 15.8 eV to higher energies. These values are in line with literature data (Oku and Hirokawa, 1976; Shi et al., 2012). An Auger peak was detected at $\sim 774\text{ eV}$ (Wagner, 1972). The XPS spectra of both compounds shows satellite features of Co $2p_{3/2}$ (shifted by 4.4 eV) and Co $2p_{1/2}$ (shifted by 5.9 eV), respectively. The satellite peaks in the Co $2p$ region are due to high-spin Co^{2+} ions, whereas low-spin Co^{3+} ions have no or very weak satellite peaks (Frost et al., 1974; Shi et al., 2012). To distinguish the configuration of the Co centers, the ratio between areas of Co $2p$ peak and the satellite is determined. For compound **1**, the Co $2p$:satellite area ratio is around 1, for compound **1-A** the ratio decreases to 0.8. This means that, for compound **1-A**, the satellite peak is stronger and more high-spin Co^{2+} ions are present.

Magnetism and Magnetochemical Modeling

As the magnetic ac susceptibility data did not reveal significant out-of-phase signals at low temperatures, the magnetic properties of compounds **1** and **2** are analyzed in terms of their magnetic dc susceptibility. The magnetic data of **1** are shown as $\chi_m T$ vs. T and M_m vs. B plots in **Figure 6**. These data are corrected for diamagnetic contributions as well as the temperature-independent paramagnetic (TIP) contributions originating from the four octahedrally coordinated low-spin Co^{III} centers. The value of $\chi_m T = 2.87\text{ cm}^3\text{ K mol}^{-1}$ at 290 K is within the

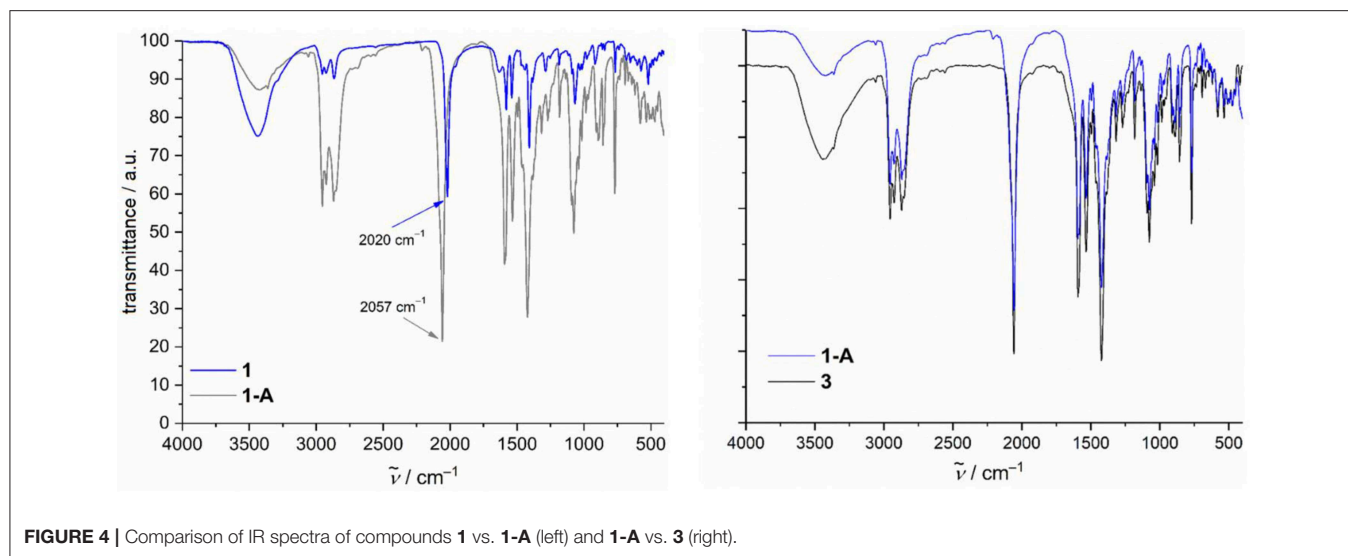
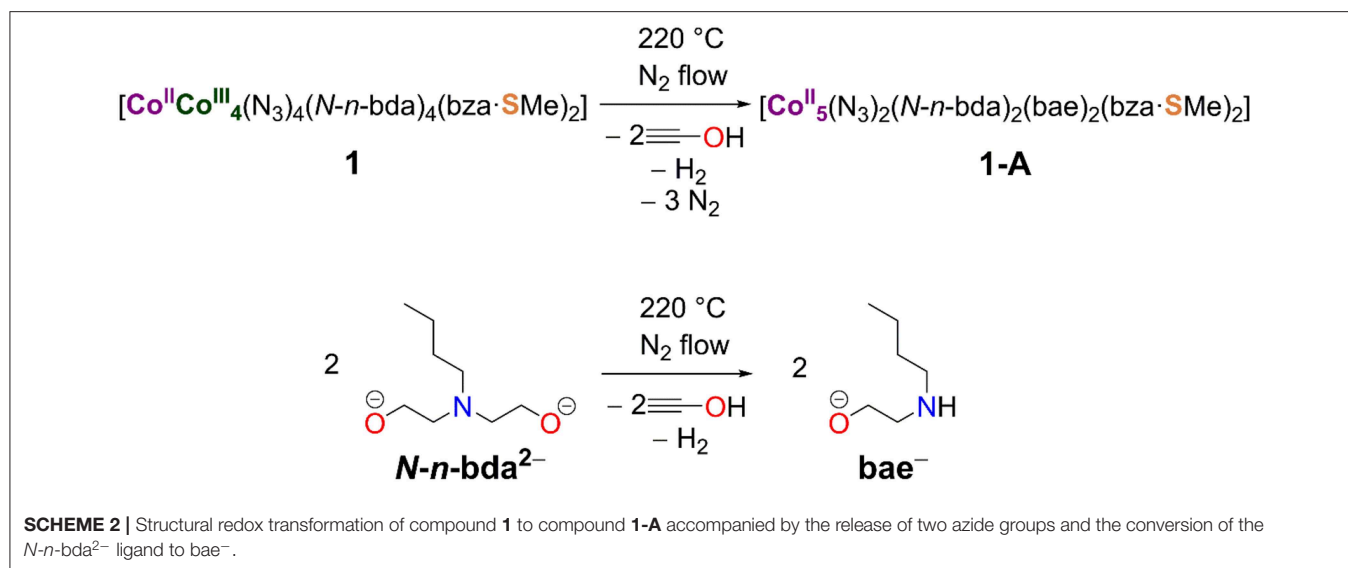


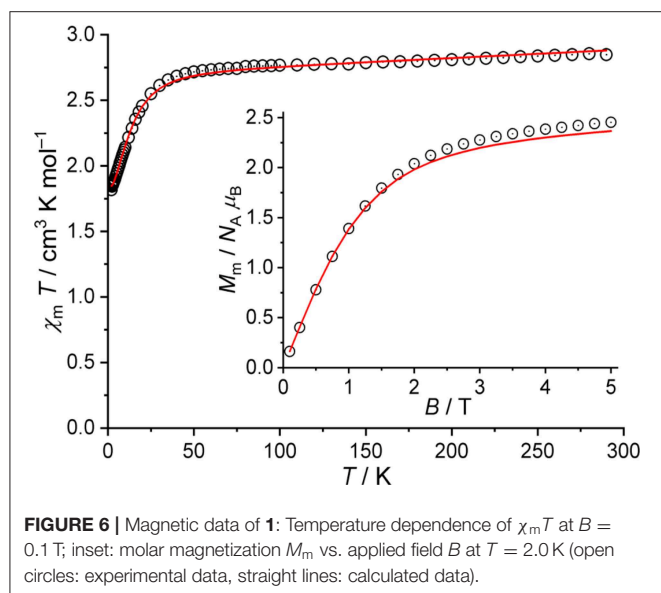
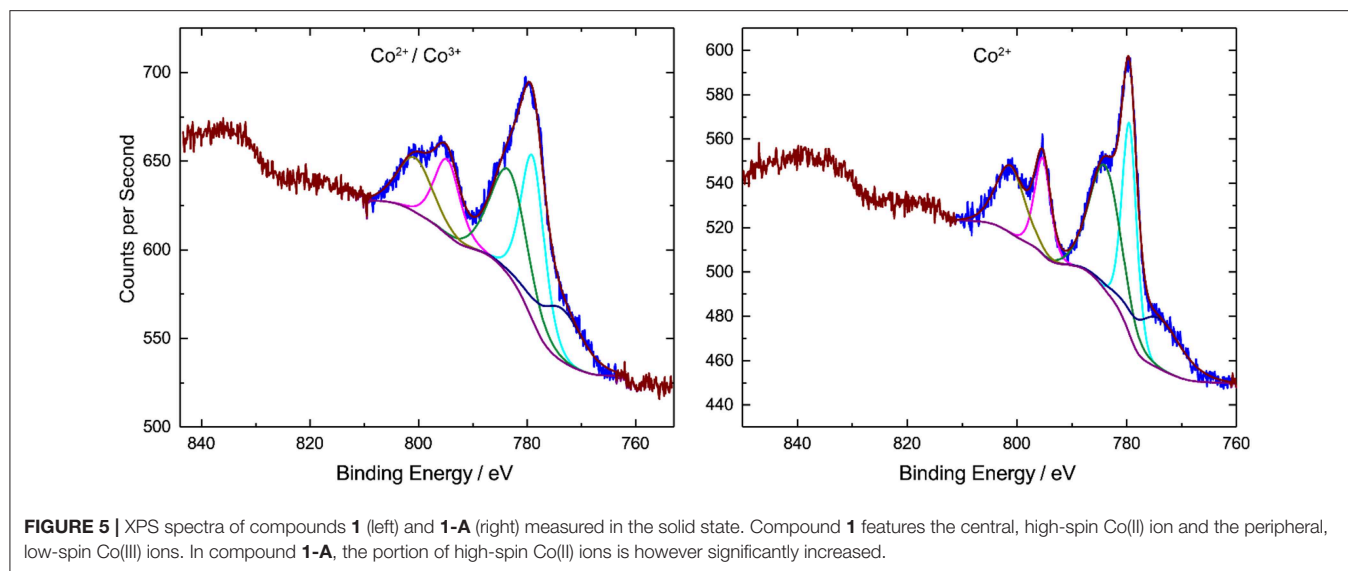
FIGURE 4 | Comparison of IR spectra of compounds **1** vs. **1-A** (left) and **1-A** vs. **3** (right).



range $2.31\text{--}3.38 \text{ cm}^3 \text{ K mol}^{-1}$ expected for a single high-spin Co^{II} center (Lueken, 1999). Upon lowering the temperature, $\chi_m T$ remains almost constant and marginally decreases down to a temperature of 50 K. This spin-like behavior is due to the orbital singlet 4A_2 ground term of tetrahedrally coordinated $3d^7$ centers. The strong distortion of the tetrahedral coordination geometry is revealed at temperatures smaller than 50 K, at which $\chi_m T$ rapidly decreases, reaching $1.83 \text{ cm}^3 \text{ K mol}^{-1}$ at 2.0 K. The characteristics of this interval are due thermal depopulation of the energy states, namely, the splitting of the 4A_2 ground term (into two Kramers doublets) caused primarily by ligand field effects and spin-orbit coupling. This is also reflected in the dependence of the molar magnetization on the applied magnetic field at 2.0 K. The molar magnetization M_m is a linear function of B up to *ca.* 1 T, and reaches $\sim 2.5 N_A \mu_B$ at 5 T without being saturated. Therefore, magnetic data are in agreement with

a single high-spin Co^{II} center ($3d^7$) in a distorted tetrahedral ligand field.

The computational framework CONDON (Schilder and Lueken, 2004; Speldrich et al., 2011, 2018) was used to analyze the magnetic data of **1** in more detail. Standard values (Griffith, 1971) for the Racah parameters ($B = 1,115 \text{ cm}^{-1}$, $C = 4,366 \text{ cm}^{-1}$) and the one-electron spin-orbit coupling constant ($\zeta_{3d} = 533 \text{ cm}^{-1}$) are used to analyze the Co^{II} center using the “full” basis of microstates of a d^7 valence electron configuration (120 microstates). The least-squares fit with an SQ of 1.5% (relative root mean square error) yields the ligand field parameters $B_0^2 = (-15,460 \pm 250) \text{ cm}^{-1}$, $B_0^4 = (-9,782 \pm 411) \text{ cm}^{-1}$, $B_4^4 = (-4,634 \pm 512) \text{ cm}^{-1}$ (Wybourne notation, D_{2d} symmetric ligand field) and $\lambda_{\text{mf}} = (65 \pm 1) \times 10^{-3} \text{ mol cm}^{-3}$. The magnitude of the molecular field parameter λ_{mf} corresponds to minimal intermolecular ferromagnetic exchange interactions



($zJ \approx 0.02\text{--}0.03\text{ cm}^{-1}$), which has been introduced due to the slight change of the curvature of $\chi_m T$ for $T < 4$ K, and can be considered as negligible. The modeled data are displayed in **Figure 6** as solid lines. According to the fit parameters, the ligand field is represented by a strongly compressed tetrahedron. The tetrahedral 4A_2 ground term of the free ion splits into two Kramers doublets, which are separated by an energy gap of 32 cm^{-1} . The second excited doublet (derived from the 4T_2 term of the undistorted tetrahedral symmetry) is located at $2,100\text{ cm}^{-1}$ relative to the ground doublet, revealing a good isolation of the two ground doublets in agreement with the observed spin-like behavior of $\chi_m T$ in the temperature range $50\text{--}290$ K.

The $\chi_m T$ vs. T and M_m vs. B plots of **2** are shown in **Figure 7**. These data are corrected for diamagnetic contributions

and TIP contributions of the two octahedrally coordinated low-spin Co^{III} centers. At 290 K , the value of $\chi_m T$ is $11.93\text{ cm}^3\text{ K mol}^{-1}$, which is well within the range $9.25\text{--}13.53\text{ cm}^3\text{ K mol}^{-1}$ expected (Lueken, 1999) for four non-interacting high-spin Co^{II} centers. Upon cooling the compound, $\chi_m T$ gradually decreases with a distinct change of the slope at about 100 K , reaching a minimum of $8.08\text{ cm}^3\text{ K mol}^{-1}$ at 7.0 K . Subsequently, $\chi_m T$ slightly increases to a maximum of $8.18\text{ cm}^3\text{ K mol}^{-1}$ at 2.4 K , and drops to $8.07\text{ cm}^3\text{ K mol}^{-1}$ at 2.0 K . At this temperature, the molar magnetization rapidly increases for fields below 2 T , and subsequently slowly grows to $8.6 N_A \mu_B$ at 5.0 T without reaching saturation. (Distorted) octahedral Co^{II} centers are not spin-like, but show a temperature-dependent $\chi_m T$ behavior due to considerable contributions from the unquenched orbital momentum. This is mainly due to a significant mixing of the $^4T_{1g}(^4F)$ ground term with the excited $^4T_{1g}(^4P)$ term caused by spin-orbit coupling. Therefore, the decrease of $\chi_m T$ with decreasing temperatures is basically due to these single-ion effects, and only to a minor degree due to potential exchange interactions. The existence of the latter can be derived from the occurrence of the minimum, which is indicative of ferromagnetic exchange interactions. However, these interactions are weak, since the minimum is at quite low temperatures, and the increase upon further cooling is rather small. Additionally, even weaker antiferromagnetic exchange interactions could be present based on the small drop off of $\chi_m T$ at $T \leq 2.4\text{ K}$, although also the Zeeman effect yields a relevant contribution to $\chi_m T$ at 0.1 T in this temperature range.

For **2**, we adopt the same values for the Racah parameters B and C as well as the one-electron spin-orbit coupling constant ζ_{3d} as for **1**, using the “full” basis of microstates of the d^7 valence electron configuration per Co^{II} center. Due to structural information, the ligand field of each center is approximated to C_{4v} symmetry, and all four centers are taken to be roughly the same. For the exchange interactions pathways, we set the exchange interactions between $\text{Co6}\text{--Co1}$ and $\text{Co6}\text{--Co5}$ to J_1

(Co6 is the central Co^{II} center, Co1 and Co5 are the peripheral Co^{II} in a NO₅-coordination environment), and between Co6–Co3 to J_2 . For the calculation of the exchange interactions, the basis is reduced to the 12 energy states of the $^4T_{1g}$ term for each center. The least-squares fit ($SQ = 0.9\%$) yields the ligand field parameters $B_0^2 = (-7,957 \pm 136) \text{ cm}^{-1}$, $B_0^4 = (24,378 \pm 126) \text{ cm}^{-1}$, and $B_4^4 = (19,403 \pm 139) \text{ cm}^{-1}$, and the exchange interaction parameters $J_1 = (0.38 \pm 0.04) \text{ cm}^{-1}$ and $J_2 = (-0.29 \pm 0.03) \text{ cm}^{-1}$ (Heisenberg-Hamiltonian in “ $-2J$ ” notation). Hence, the ligand field parameters describe the field of an elongated octahedron as an approximation for all four Co^{II} centers. Two exchange pathways are characterized by weak ferromagnetic exchange interactions (J_1), while the remaining pathway is characterized by a weak antiferromagnetic exchange interaction (J_2). The corresponding fit is shown as a solid line in Figure 7.

The magnetic properties of **1-A** (compound **1** after thermal treatment) are shown as $\chi_m T$ vs. T and M_m vs. B plots in Figure 8 (open circles). The curves of **1** and **1-A** distinctly differ from each other: The $\chi_m T$ value of **1-A** at 290 K is $13.69 \text{ cm}^3 \text{ K mol}^{-1}$, which represents a value well within the expected range $11.56\text{--}16.91 \text{ cm}^3 \text{ K mol}^{-1}$ for five non-interacting high-spin Co^{II} centers (Lueken, 1999) assuming a similar or nearly similar structure of **1-A** as for **1**. Upon decreasing temperature, $\chi_m T$ continuously decreases with a distinct change of the slope at about 100 K characteristic for octahedrally coordinated high-spin Co^{II} centers. At lower temperatures, we observe a minimum at 25 K, a maximum of $12.00 \text{ cm}^3 \text{ K mol}^{-1}$ at 7.0 K, and subsequently a sharp drop to $10.53 \text{ cm}^3 \text{ K mol}^{-1}$ at 2.0 K. Therefore, the $\chi_m T$ vs. T curve below 30 K reveals the presence of weak or moderate exchange interactions of both kinds: Ferromagnetic due to the observed minimum, and antiferromagnetic due to the pronounced drop off for $T < 7.0$ K. The molar magnetization at 2.0 K rapidly increases at fields

below 0.5 T and continues to increase to $6.3 N_A \mu_B$ at 5.0 T without reaching saturation, which is characteristic of high-spin octahedral Co^{II} centers.

Given the striking similarities in the IR spectra of **1-A** and **3** (Figure 4), we show the $\chi_m T$ vs. T curve and M_m vs. B curve of **3** in addition to the data of **1-A** in Figure 8. At 290 K, $\chi_m T$ of **3** is $29.08 \text{ cm}^3 \text{ K mol}^{-1}$, well with the expected (Lueken, 1999) range of $23.12\text{--}33.81 \text{ cm}^3 \text{ K mol}^{-1}$ for 10 non-interacting high-spin Co^{II} centers. Upon cooling the compound, the values of $\chi_m T$ almost linearly decrease to a minimum at 40 K, sharply increases to a maximum of $30.44 \text{ cm}^3 \text{ K mol}^{-1}$ at 5.0 K, and subsequently drops to $27.69 \text{ cm}^3 \text{ K mol}^{-1}$ at 2.0 K. The molar magnetization

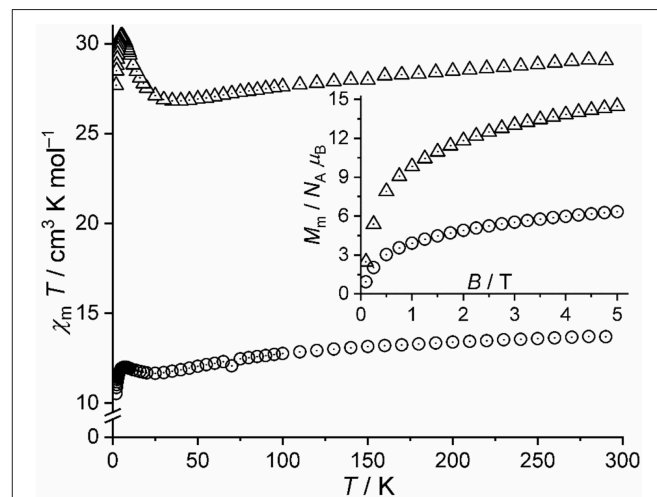


FIGURE 8 | Magnetic data of **1-A** and **3**, for comparison: Temperature dependence of $\chi_m T$ at $B = 0.1$ T; inset: molar magnetization M_m vs. applied field B at $T = 2.0$ K (open circles: **1-A**, open triangles: **3**).

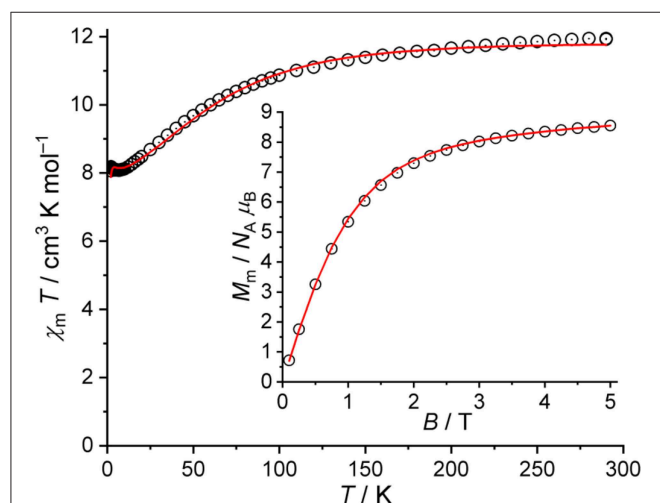


FIGURE 7 | Magnetic data of **2**: Temperature dependence of $\chi_m T$ at $B = 0.1$ T; inset: molar magnetization M_m vs. applied field B at $T = 2.0$ K (open circles: experimental data, straight lines: calculated data).

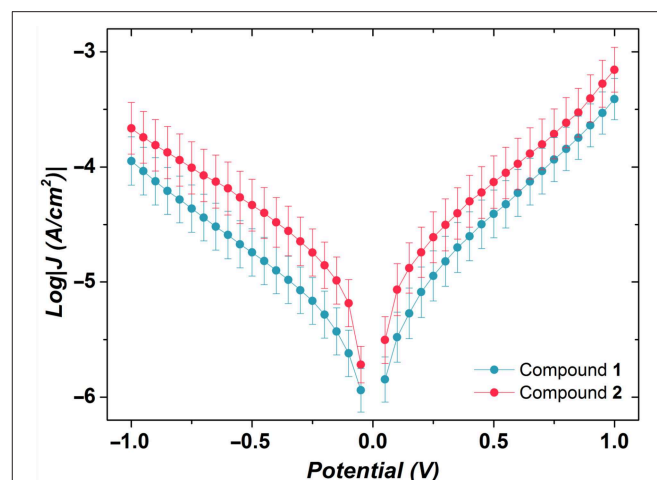


FIGURE 9 | Plots of logarithmic current-density against applied potential for the SAMs of compounds **1** and **2**. Values of $\log|J|$ at $V = 0$ V are omitted for clarity. The error bars are the 95% confidence intervals. Despite the minor difference in the shape of the J/V curves, the two SAMs are indistinguishable.

at this temperature sharply increases at fields up to 0.8 T, and subsequently increases to $14.5 N_A \mu_B$ at 5.0 T. The data of **3** are, thus, in agreement with 10 high-spin Co^{II} centers, which interact predominantly ferromagnetic, while a few exchange pathways are characterized by antiferromagnetic exchange interactions. In comparison to **1-A**, the data of **3**, however, differ significantly by more than a factor of two, show the characteristic minimum and maximum of the $\chi_m T$ curves at different temperatures with differing intensities, and have different slopes of the M_m curves at $B > 2$ T. Since also the maxima and slopes differ by a factor of two, compounds **1-A** and **3** have most likely slightly different structures and comprise different ligands, or a combination of both alternatives is present from a magnetochemical point of view.

Large-Area Charge Transport Measurements

We succeeded in growing SAMs of the target compounds **1** and **2** by immersing freshly cleaved template-stripped gold substrates (atomically smooth Au^{TS}) in a ~ 0.1 mM methanolic solution of each metal complex overnight. After rinsing with pure methanol and drying in a gentle stream of nitrogen, the SAMs were contacted with EGaIn tips to form junctions of the structure $\text{Au}^{\text{TS}}//\text{SAM}//\text{Ga}_2\text{O}_3/\text{EGaIn}$ where “/” denotes interface defined by chemisorption and “//” denotes interface defined by physisorption. Note that EGaIn is a eutectic alloy of Ga and In (75.5% Ga and 24.5% In by weight), the surface of which is covered by thin, conductive, self-limiting layer of Ga_2O_3 .

TABLE 1 | Transition voltages of compounds **1** and **2** calculated at negative and positive biases.

	V_{T}^- (V)	V_{T}^+ (V)
Compound 1	-0.56 ± 0.06	0.43 ± 0.05
Compound 2	-0.61 ± 0.07	0.50 ± 0.04

The errors are the 95% confidence intervals.

We performed an analysis of the current density–voltage (J – V) characteristics of the thus-obtained SAMs. The J – V results are illustrated in **Figure 9**. Apart from minor differences in the shape of J/V curves ($J = I/A$, where A is the area of the junction), the two SAMs are indistinguishable. By replotting J – V data in Fowler-Nordheim coordinates (transition voltage spectroscopy), it is possible to obtain information about energy level alignment inside the junction. All values of transition voltages (V_{T}) coalesce to ~ 0.6 V (**Table 1**), ~ 0.3 V higher than those reported recently for the SAMs of $\{\text{CuLn}\}$ complexes (Schmitz et al., 2018a). The featureless J – V curves shown in **Figure 9** point out single-level, non-resonant tunneling, i.e., a single potential barrier and comparably weak coupling to either electrode.

V_{T} is an approximate measure of the height of the potential barrier, which is related to level alignment, for example, the difference between the energy of the accessible frontier orbital of a molecule and the Fermi level of the electrode in an assembled junction. If a rectangular tunneling barrier is considered, the heights of the barriers in the SAMs of Co complexes are higher than those of $\{\text{CuLn}\}$ complexes (Schmitz et al., 2018a).

Similar to the SAMs of $\{\text{CuLn}\}$ complexes, Co complexes described herein can only weakly interact with the metal surface through physisorption. Thus, we expect the SAMs to be poorly ordered and the molecules are weakly coupled to the bottom electrode that is to exhibit high resistance. AFM study of the surface morphology clearly showed the presence of compounds **1** and **2**. All molecules formed monolayers on the surface of Au^{TS} and there was no sign of the multilayer formation (**Figure 10**). Moreover, the formation of SAMs increases the surface roughness of the samples, from 0.208 nm for bare Au^{TS} substrate to 0.301 nm for compound **1** and 0.282 nm for compound **2**. The obtained monolayers with an average yield of working EGaIn junctions of 91% are more electrically robust than the SAMs of previously reported $\{\text{CuLn}\}$ complexes (Schmitz et al., 2018a). This could be due to the fact that more Co complexes are generated on the surface of Au, largely reducing the space between the molecules, which contributes short contacts.

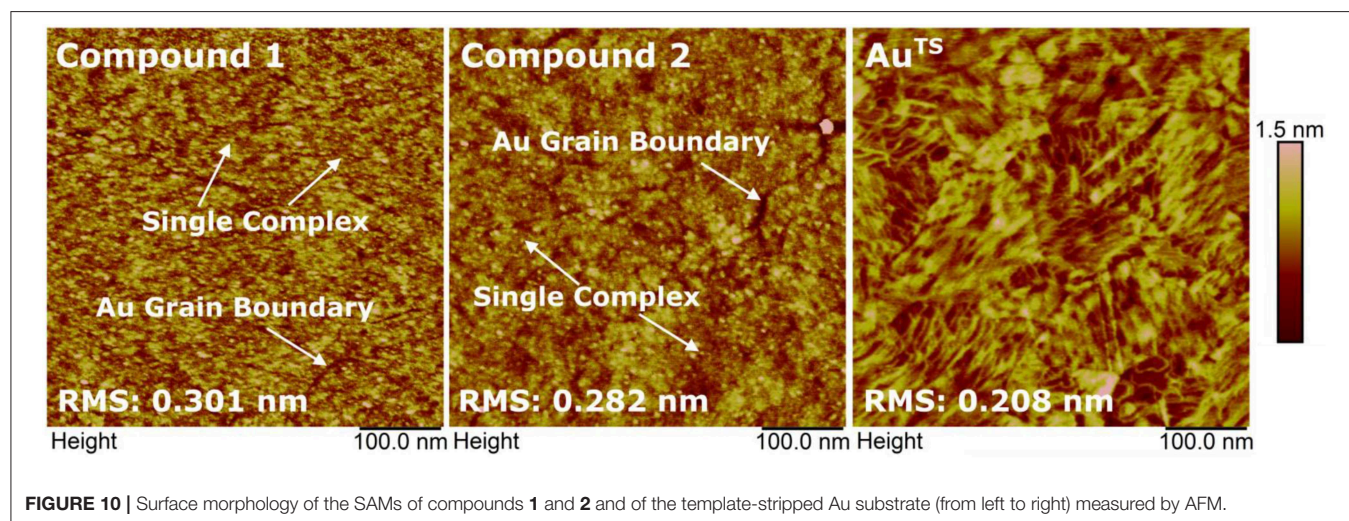


TABLE 2 | Thickness of the SAMs of compounds **1** and **2** by ellipsometry, in comparison to the dimensions of the complexes.

	Thickness (nm)	Length (nm)	Width (nm)	Height (nm)
Compound 1	1.50 ± 0.03	2.319	1.291	1.291
Compound 2	1.62 ± 0.03	1.916	2.132	1.337

Thickness Measured by Using Ellipsometry

To further characterize the SAMs grown from the target compounds, we measured the thickness of the SAMs by using ellipsometry. Three freshly prepared samples for each compound were analyzed. The average thickness is 1.50 ± 0.03 nm for compound **1** and 1.62 ± 0.03 nm for compound **2** (Table 2). It is thus in good agreement with the dimensions of the complexes (Table 2) and suggests the formation of monolayers from the studied compounds. Moreover, no presence of aggregates that exceed the size of a single complex from the morphology measured by AFM and STM was observed. Although we could not conclude the orientation of the complexes on the Au surface due to the relatively flexible ligands, the formation of SAMs from these two complexes can be ascertained.

CONCLUSION

Two novel coordination clusters, pentanuclear **1** and hexanuclear **2**, comprising high-spin Co^{II} and low-spin Co^{III} ions in the ligand environment of 4-(methylthio)benzoate ligands, fully deprotonated *N-n*-butyldiethanolamine ligands and azide ligands were synthesized and structurally characterized. Contrary to **2**, the charge-neutral compound **1** was shown to undergo reduction under solvothermal conditions to decanuclear {Co₁₀^{II}}⁻-based compound **3**. Another derivative **1-A** with only high-spin

REFERENCES

- Al-Owaedi, O. A., Bock, S., Milan, D. C., Oerthel, M.-C., Inkpen, M. S., Yufit, D. S., et al. (2017). Insulated molecular wires: inhibiting orthogonal contacts in metal complex based molecular junctions. *Nanoscale* 9, 9902–9912. doi: 10.1039/C7NR01829K
- Bu, D., Xiong, Y., Tan, Y. N., Meng, M., Low, P. J., Kuang, D.-B., et al. (2018). Understanding the charge transport properties of redox active metal-organic conjugated wires. *Chem. Sci.* 9, 3438–3450. doi: 10.1039/C7SC04727D
- Canaj, A. B., Nodaraki, L. E., Slepokura, K., Siczek, M., and Tzimopoulos, D. I., Lis, T., et al. (2014). A family of polynuclear cobalt complexes upon employment of an indeno-quinoxaline based oxime ligand. *RCS Adv.* 4, 23068–23077. doi: 10.1039/C4RA01914H
- Clark, R. C., and Reid, J. S. (1995). The analytical calculation of absorption in multifaceted crystals. *Acta Cryst.* A51, 887–897. doi: 10.1107/S0108767395007367
- Cornia, A., Mannini, M., Sainctavit, P., and Sessoli, R. (2011). Chemical strategies and characterization tools for the organization of single molecule magnets on surfaces. *Chem. Soc. Rev.* 40, 3076–3091. doi: 10.1039/C0CS00187
- Cossee, P. (1958). Magnetic properties of cobalt in oxide lattices. *J. Inorg. Nucl. Chem.* 8, 483–488. doi: 10.1016/0022-1902(58)80218-3

Co^{II} ions was isolated after thermogravimetric treatment of **1**, although its structure could not be elucidated due to the lack of availability of single crystals suitable for X-ray diffraction. The molecular deposition of compounds **1** and **2** from solution on gold surfaces resulted in the formation of physisorbed SAMs that revealed higher electrical robustness than SAMs consisting of the previously reported {Cu^{II}Ln^{III}} complexes (Schmitz et al., 2018a). Further studies are however needed to showcase the potential of polynuclear cobalt complexes to switch between different stable metal-based oxidation or spin states by application of external stimuli (Xin et al., 2019) as temperature, light, or magnetic fields.

DATA AVAILABILITY STATEMENT

All datasets generated for this study are included in the article/Supplementary Material.

AUTHOR CONTRIBUTIONS

All authors listed have made a substantial, direct and intellectual contribution to the work, and approved it for publication.

ACKNOWLEDGMENTS

XQ and RC acknowledge the Zernike Institute for Advanced Materials for financial support. The authors are grateful to Dr. B. Santiago-Schübel (Forschungszentrum Jülich) for ESI-MS measurements.

SUPPLEMENTARY MATERIAL

The Supplementary Material for this article can be found online at: <https://www.frontiersin.org/articles/10.3389/fchem.2019.00681/full#supplementary-material>

- Dreiser, J. (2015). Molecular lanthanide single-ion magnets: from bulk to submonolayers. *J. Phys. Condens. Matter* 27:183203. doi: 10.1088/0953-8984/27/18/183203
- Dreiser, J., Ako, A. M., Wäckerlin, C., Heidler, J., Anson, C. E., Powell, A. K., et al. (2015). Reduction of Mn₁₉ Coordination Clusters on a Gold Surface. *J. Phys. Chem. C* 119, 3550–3555. doi: 10.1021/jp510240b
- Englert, U., and Strähle, J. (1987). Crystal structure of Co(acac)₂(NO) and its oxidation products Co(acac)₂(NO₂)(H₂O) and Co₅(acac)₈(μ₃-OH)₂(μ-N,O-NO₂)₂. *Z. Naturforsch.* 42b, 959–966.
- Ferguson, A., Parkin, A., and Murrie, M. (2006). Synthesis and structural characterisation of polynuclear cobalt complexes with partially-deprotonated Bis-tris. *Dalton Trans.* 3627–3628. doi: 10.1039/B603622H
- Frost, D. C., McDowell, C. A., and Woolsey, I. S. (1974). X-ray photoelectron spectra of cobalt compounds. *Mol. Phys.* 27, 1473–1489. doi: 10.1080/00268977400101251
- Funes, A. V., Carrella, L., Sorace, L., Rentschler, E., and Alborés, P. (2015). Switching nuclearity and Co(II) content through stoichiometry adjustment: {Co^{II}Co^{III}} and {Co^{II}Co^{III}} mixed valent complexes and a study of their magnetic properties. *Dalton Trans.* 44, 2390–2400. doi: 10.1039/C4DT03034F
- Ghisolfi, A., Monakhov, K. Y., Pattacini, R., Braunstein, P., López, X., de Graaf, C., et al. (2014). A comparative synthetic, magnetic and theoretical study of

- functional M_4Cl_4 cubane-type Co(II) and Ni(II) complexes. *Dalton Trans.* 43, 7847–7859. doi: 10.1039/C4DT00306C
- Griffith, J. S. (1971). *The Theory of Transition-Metal Ions*. Cambridge: Cambridge University Press.
- Higgins, S. J., and Nichols, R. J. (2018). Metal/molecule/metal junction studies of organometallic and coordination complexes; what can transition metals do for molecular electronics? *Polyhedron* 140, 25–34. doi: 10.1016/j.poly.2017.10.022
- Li, Y.-W., Guo, L.-Y., Feng, L., Jagličić, Z., Zeng, S.-Y., and Sun, D. (2017). Self-assembly, structures, magnetic properties and solution behaviors of six mixed-valence cobalt clusters. *CrystEngComm*. 19, 5897–5906. doi: 10.1039/C7CE01375B
- Linnenberg, O., Moors, M., Notario-Estévez, A., López, X., de Graaf, C., Peter, S., et al. (2018). Addressing multiple resistive states of polyoxovanadates: conductivity as a function of individual molecular redox states. *J. Am. Chem. Soc.* 140, 16635–16640. doi: 10.1021/jacs.8b08780
- Lueken, H. (1999). *Magnetochemie*. Stuttgart: B. G. Teubner Verlag.
- Maloth, S., Kurapati, S. K., and Pal, S. (2015). Synthesis, structure, and properties of a pentanuclear cobalt(III) coordination cluster. *J. Coord. Chem.* 68, 1402–1411. doi: 10.1080/00958972.2015.1018195
- Mandal, S., Mondal, S., Rajnák, C., Titiš, J., Boča, R., and Mohanta, S. (2017). Syntheses, crystal structures and magnetic properties of two mixed-valence Co(III)Co(II) compounds derived from Schiff base ligands: field-supported single-ion-magnet behavior with easy-plane anisotropy. *Dalton Trans.* 46, 13135–13144. doi: 10.1039/C7DT02455J
- Mitcov, D., Pedersen, A. H., Ceccato, M., Gelardi, R. M., Hassenkam, T., Konstantatos, A., et al. (2019). Molecular multifunctionality preservation upon surface deposition for a chiral single-molecule magnet. *Chem. Sci.* 10, 3065–3073. doi: 10.1039/C8SC04917C
- Oku, M., and Hirokawa, K. (1976). X-ray photoelectron spectroscopy of Co_3O_4 , Fe_3O_4 , Mn_3O_4 , and related compounds. *J. Electron Spectrosc. Relat. Phenom.* 8, 475–481. doi: 10.1016/0368-2048(76)80034-5
- Parks, J. J., Champagne, A. R., Costi, T. A., Shum, W. W., Pasupathy, A. N., Neuscamman, E., et al. (2010). Mechanical control of spin states in spin-1 molecules and the underscreened Kondo effect. *Science* 328, 1370–1373. doi: 10.1126/science.1186874
- Ray, U., Chand, B., Mostafa, G., Cheng, J., Lu, T.-H., and Sinha, C. (2003). Mono- and binuclear cobalt(II)-azido complexes of arylazoimidazole: synthesis, spectral characterization, electrochemistry and crystal structure. *Polyhedron* 22, 2587–2594. doi: 10.1016/S0277-5387(03)00347-4
- Reus, W. F., Thuo, M. M., Shapiro, N. D., Nijhuis, C. A., and Whitesides, G. M. (2012). The SAM, not the electrodes, dominates charge transport in metal-monolayer// Ga_2O_3 /gallium–indium eutectic junctions. *ACS Nano* 6, 4806–4822. doi: 10.1021/nn205089u
- Scheurer, A., Ako, A. M., Saalfrank, R. W., Heinemann, F. W., Hampel, F., Petukhov, K., et al. (2010). Synthesis, magnetic properties, and STM spectroscopy of cobalt(II) cubanes $[Co_4^II(Cl)_4(HL)_4]$. *Chem. Eur. J.* 16, 4784–4792. doi: 10.1002/chem.200902578
- Schilder, H., and Lueken, H. (2004). Computerized magnetic studies on d, f, d–d, f–f, and d–S, f–S systems under varying ligand and magnetic fields. *J. Magn. Magn. Mat.* 281, 17–26. doi: 10.1016/j.jmmm.2004.03.041
- Schmitz, S., Izarova, N. V., Besson, C., van Leusen, J., Kögerler, P., and Monakhov, K. Y. (2019). Ion-directed coordinative polymerization of copper(II) pyridyl-alcohol complexes through thiane functionalities. *Z. Anorg. Allg. Chem.* 645, 409–415. doi: 10.1002/zaac.201800469
- Schmitz, S., Kovalchuk, A., Martín-Rodríguez, A., van Leusen, J., Izarova, N. V., Bourone, S. D. M., et al. (2018a). Element-selective molecular charge transport characteristics of binuclear copper(II)-lanthanide(III) complexes. *Inorg. Chem.* 57, 9274–9285. doi: 10.1021/acs.inorgchem.8b01279
- Schmitz, S., Monakhov, K. Y., van Leusen, J., Izarova, N. V., Heß, V., and Kögerler, P. (2016a). $\{Co_5^{II/III}\}$ horseshoe and $\{Ni_4^{II}\}$ lacunary cubane coordination clusters: The isobutyrate/*N*-butyldiethanolamine reaction system. *RSC Adv.* 6, 100664–100669. doi: 10.1039/C6RA19232G
- Schmitz, S., Secker, T., Batool, M., van Leusen, J., Nadeem, M. A., and Kögerler, P. (2018b). A planar decanuclear cobalt(II) coordination cluster. *Inorg. Chim. Acta* 482, 522–525. doi: 10.1016/j.ica.2018.06.005
- Schmitz, S., van Leusen, J., Ellern, A., Kögerler, P., and Monakhov, K. Y. (2015). A thioether-decorated $\{Mn_{11}Tb_4\}$ coordination cluster with slow magnetic relaxation. *Inorg. Chem. Front.* 2, 1095–1100. doi: 10.1039/C5QI0172B
- Schmitz, S., van Leusen, J., Ellern, A., Kögerler, P., and Monakhov, K. Y. (2016b). Thioether-terminated nickel(II) coordination clusters with $\{Ni_6\}$ horseshoe- and $\{Ni_8\}$ rollercoaster-shaped cores. *Inorg. Chem. Front.* 3, 523–531. doi: 10.1039/C5QI00278H
- Schmitz, S., van Leusen, J., Izarova, N. V., Bourone, S. D. M., Ellern, A., Kögerler, P., et al. (2018c). Triangular $\{Ni_3\}$ coordination cluster with a ferromagnetically coupled metal-ligand core. *Polyhedron* 144, 144–151. doi: 10.1016/j.poly.2018.01.014
- Schmitz, S., van Leusen, J., Izarova, N. V., Lan, Y., Wernsdorfer, W., Kögerler, P., et al. (2016c). Supramolecular 3d-4f single-molecule magnet architectures. *Dalton Trans.* 45, 16148–16152. doi: 10.1039/C6DT03392J
- Sheldrick, G. M. (2015). Crystal structure refinement with SHELXL. *Acta Cryst.* C71, 3–8. doi: 10.1107/S2053229614024218
- Shi, R., Chen, G., Ma, W., Zhang, D., Qiu, G., and Liu, X. (2012). Shape-controlled synthesis and characterization of cobalt oxides hollow spheres and octahedra. *Dalton Trans.* 41, 5981–5987. doi: 10.1039/C2DT12403C
- Speldrich, M., Schilder, H., Lueken, H., and Kögerler, P. (2011). A computational framework for magnetic polyoxometalates and molecular spin structures: CONDON 2.0. *Isr. J. Chem.* 51, 215–227. doi: 10.1002/ijch.201100013
- Speldrich, M., van Leusen, J., and Kögerler, P. (2018). CONDON 3.0: an updated software package for magnetochemical analysis—all the way to polynuclear actinide complexes. *J. Comput. Chem.* 39, 2133–2145. doi: 10.1002/jcc.25389
- Sun, L., Diaz-Fernandez, Y. A., Gschneidner, T. A., Westerlund, F., Lara-Avila, S., and Moth-Poulsen, K. (2014). Single-molecule electronics: from chemical design to functional devices. *Chem. Soc. Rev.* 43, 7378–7411. doi: 10.1039/C4CS00143E
- Wagner, C. D. (1972). Auger lines in x-ray photoelectron spectrometry. *Anal. Chem.* 44, 967–973. doi: 10.1021/ac60314a015
- Wang, G., Kim, T.-W., and Lee, T. (2011). Electrical transport characteristics through molecular layers. *J. Mater. Chem.* 21, 18117–18136. doi: 10.1039/C1JM12702K
- Xin, N., Guan, J., Zhou, C., Chen, X., Gu, C., Li, Y., et al. (2019). Concepts in the design and engineering of single-molecule electronic devices. *Nature Rev. Phys.* 1, 211–230. doi: 10.1038/s42254-019-0022-x
- Yan, L., and Seminario, J. M. (2005). Electronic structure and electron transport characteristics of a cobalt complex. *J. Phys. Chem. A* 109, 6628–6633. doi: 10.1021/jp052798k
- Yao, Y. F., Zhang, L., Orgiu, E., and Samori, P. (2019). Unconventional nanofabrication for supramolecular electronics. *Adv. Mater.* 31:1900599. doi: 10.1002/adma.201900599

Conflict of Interest: The authors declare that the research was conducted in the absence of any commercial or financial relationships that could be construed as a potential conflict of interest.

Copyright © 2019 Schmitz, Qiu, Glöß, van Leusen, Izarova, Nadeem, Griebel, Chiechi, Kögerler and Monakhov. This is an open-access article distributed under the terms of the Creative Commons Attribution License (CC BY). The use, distribution or reproduction in other forums is permitted, provided the original author(s) and the copyright owner(s) are credited and that the original publication in this journal is cited, in accordance with accepted academic practice. No use, distribution or reproduction is permitted which does not comply with these terms.